國 立 交 通 大 學

電子工程學系　電子研究所碩士班

碩 士 論 文

矽及鍺通道 P 型金氧半電晶體二維量子井模擬

Subband Structures of Silicon and Germanium Channels in P-type Metal-oxide-semiconductor Devices

研 究 生 ：邱子華

指導教授 ：汪大暉 博士

中華民國 九十七 年 七 月

矽及鍺通道P型金氧半電晶體

二維量子井模擬

Subband Structures of Silicon and Germanium Channels in P-type Metal-oxide-semiconductor Devices

研 究 生：邱子華　　Student :Tzu-Hua Chiu

指導教授：汪大暉 博士　　Advisor : Dr. Tahui Wang

國立交通大學

電子工程學系 電子研究所碩士班

碩士論文

A Thesis

Submitted to Department of Electronics Engineering & Institute of Electronics

College of Electrical and Computer Engineering

National Chiao Tung University

In Partial Fulfillment of the Requirements

For the Degree of Master

In

Electronic Engineering

July 2008

Hsinchu, Taiwan, Republic of China.

中華民國 九十七 年 七 月

矽及鍺通道金氧半電晶體二維量子井模擬

學生：邱子華　　指導教授：汪大暉 博士

國立交通大學 電子工程學系 電子研究所

摘要

目前，利用由製程所造成的單軸應力(uniaxial stress)來改善元件效能已經被廣泛地使用，例如矽鍺源汲極、接觸孔蝕刻停止層。而採用高載子遷移率的鍺通道或應變鍺通道，對於未來 CMOS 微縮是必要的。所以研究因形變而改變的載子傳導帶或價電帶結構是個重要的議題。

在本篇論文中，吾人利用 Luttenger-Kohn 模型計算價電帶結構，自洽計算薛丁格及泊松方程式，其中包含矽及鍺通道金氧半電晶體二維量子井。最後，吾人利用蒙地卡羅(Monte Carlo)方法來模擬量子井中電洞的傳輸。

Subband Structures of Silicon and Germanium Channels in P-type Metal-oxide-semiconductor Devices

Student: Tzu-Hua Chiu Advisor: Dr. Tahui Wang

Department of Electronics Engineering

& Institute of Electronics

National Chiao Tung University

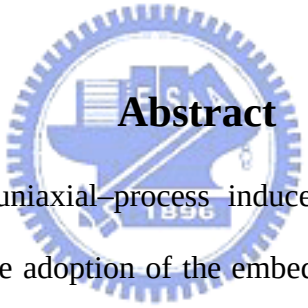

Abstract

For today's technology, uniaxial–process induced stress is used to improve device performance. One method is the adoption of the embedded and raised SiGe in the p-channel source and drain and a tensile capping layer on the n-channel device. The other method is with advantages of dual stress liners: compressive and tensile silicon nitride (SiN) for p- and n-channel devices, respectively. However, for further CMOS scaling, it is imperative to investigate other high mobility channel materials, such as Ge, strained Si/Ge and GaAs. Due to the complexity of the coupling valence band among the heavy, light and split-off bands, the treatment of one mass approximation applied to hole quantization in semiconductor inversion layer is incorrect. This thesis focuses on valence band calculations in various devices, such as Si MOS structure and double gate devices by iteratively solving the coupled Schrödinger and Poisson equations with six-band Luttinger-Kohn model. Finally, we developed a two-dimensional Monte Carlo simulation to study hole transport properties in SiGe and Ge quantum wells.

Acknowledgements

The author wishes to express his deep feeling of gratitude to his advisor, Professor Tahui Wang, for his patient guidance, encouragement, supports and insight during the course of this study. Moreover, the author wants to thank the members of the DSML; C. J. Tang, J. P. Chiou for their useful discussions and teaching.

Finally, the author gives the greatest appreciation to his family for their love and care during growing and developing, which makes the author become a mature and brave person.

Contents

Table Captions

Figure Captions

Chapter 1

Introduction

For the past decades, the scaling of silicon complementary metal-oxide semiconductor (CMOS) transistor has enabled not only an exponential increase in integration circuit density, but also a corresponding enhancement in the transistor performance. But as the transistor gate length shrinks down to 35nm [1.1, 1.2], physical limitations, such as off-state leakage current and power density, make geometric scaling an increasingly challenging task. Therefore, new techniques are required to improve transistor's performance. The key feature to enhance 90-, 65-, and 45-nm technology nodes is uniaxial-process induced stress [1.3-1.5]. For p-type MOSFETs, the embedded $Si_{1-x}Ge_x$ in source and drain area was promoted by Intel [1.6]. For the counterpart of n-type MOSFETs, a tensile silicon nitride-capping layer was used to enhance electron mobility. However, for further CMOS scaling, it is imperative to investigate other high mobility channel materials, such as Ge, strained Si/Ge and GaAs [1.7, 1.8], which may possess better carrier transport property than a highly strained Si. As we know, the device performance can be affected through the band structure, which determines the scattering rates and density of states. As a consequence, the purpose of this thesis is to understand the band structure characteristics of these devices, especially for the case of complicated valence bands. In addition, carrier mobility can be further improved in quantum structure MOSFETs owing to the modification of a band-structure and carrier scattering rates. The valence subband structures of various devices, such as Ge quantum well, Si metal-oxide-semiconductor structure and double gate devices, are included in this thesis to provide subband structures, wave functions and density of states to study the behavior of the carrier transport by a Monte Carlo simulation.

The organization of the thesis is in the following.

In chapter 2, the valence band structures are calculated by using a Luttinger-Kohn model. The 30 Å infinite quantum well of Si and Ge are compared.

In chapter 3, we examine the main features of a two-dimensional hole gas confined near a Si and SiO_2 interface. The six-band Luttinger-Kohn model is used to study the band warping of the heavy-hole, light-hole and split-off bands. Moreover, we solve iteratively and simultaneously the Schrödinger and Poisson equations in the case of an inversion of holes in a P-channel metal-oxide-semiconductor structure for different gate biases. The simulated subband energies suggest that the use of one mass approximation in each subband is incorrect. Furthermore, the simulation results showed that the character of the subbands becomes mixed as the wave-vector $k_{//}$ separates from zero. We also compare the main characteristics of the inversion layer on (001) and (110) substrates.

In chapter 4, the self-consistent solution of Schrödinger and Poisson equation is applied to single and double gate metal-oxide-semiconductor (MOS) structures. The influence of the semiconductor film thickness of the single and double gate MOS on the hole concentration distribution, inversion hole density, threshold voltage and transverse effective electric field is analyzed. The simulations results show that the transverse effective is lower in the double gate device compared to that in the single gate device, which possibly leads to improved mobility as a result of a reduction of the surface roughness scattering.

In chapter 5, we developed a two dimensional hole Monte Carlo simulation to study the hole transport in Ge and SiGe quantum wells. The intra and inter subband scattering rate are evaluated based on the Fermi-golden rule. The simulation results show that the phonon-limited low-field mobility in Ge quantum well is larger that that in SiGe quantum well due to lower scattering rate and lower effective mass. The

temperature dependence of mobility is also demonstrated.

Finally, a brief conclusion will be given in chapter 6.

Chapter 2

The Luttinger-Kohn Model

2.1 Introduction

Various methods have been developed to calculate a band structure in semiconductors. These methods can be grouped into four categories: the pseudopotential method [2.1,2.2], the envelope-function (k · p) method [2.3], the tight binding method [2.4], and the bond orbital model (BOM) method [2.5,2.6]. Among these methods, the pseudopotential approach is suitable for a conduction band structure and the k · p method is widely used to calculate a valence band structure. As a contrast, although the tight binding method can take the effect of a full valence band structure into account, the main disadvantage of this method is that it requires many empirical parameters which are usually determined by tedious fitting procedures. In this thesis, we calculate the valence band structure using the envelope function method. As we know, in the Kane's model, as shown in Fig. 2.1 (a) and (b), only a conduction band, a heavy-hole, a light-hole and a split-off band with double degeneracy are taken into account. Other higher and lower bands are not considered, which results in an incorrect effective mass for the heavy-hole band. On the other hand, in the Luttinger-Kohn model, the heavy-hole, the light-hole and split-off bands in double degeneracy are considered and are called class A. All other bands are defined as class B. The effects of bands in class B on those in class A are included in the Luttinger-Kohn model.

In chapter 2, in order to take into account the effect of uniaxial compressive strain, the Luttinger-Kohn model is used. This model is similar to the k · p method.

The strain effects can be included with the Bir-Pikus deformation potentials. The Luttinger-Kohn model is described as follows.

2.2 Valence Band Structure Calculation

2.2.1 The Luttinger-Kohn Model

Based on the theory of Luttinger-Kohn and Bir-Pikus [2.7], the valence band structure of a strained bulk material can be derived by the following Hamiltonian in the envelope-function space:

$$H^{LK} = -\begin{bmatrix} P+Q & -S & R & 0 & -\frac{1}{\sqrt{2}}S & \sqrt{2}R \\ -S^{+} & P-Q & 0 & R & -\sqrt{2}Q & \sqrt{\frac{3}{2}}S \\ R^{+} & 0 & P-Q & S & \sqrt{\frac{3}{2}}S^{+} & \sqrt{2}Q \\ 0 & R^{+} & S^{+} & P+Q & -\sqrt{2}R^{+} & -\frac{1}{\sqrt{2}}S^{+} \\ -\frac{1}{\sqrt{2}}S^{+} & -\sqrt{2}Q^{+} & \sqrt{\frac{3}{2}}S & -\sqrt{2}R & P+\Delta & 0 \\ \sqrt{2}R^{+} & \sqrt{\frac{3}{2}}S^{+} & \sqrt{2}Q^{+} & -\frac{1}{\sqrt{2}}S & 0 & P+\Delta \end{bmatrix} \begin{matrix} \left|\frac{3}{2},\frac{3}{2}\right\rangle \\ \left|\frac{3}{2},\frac{1}{2}\right\rangle \\ \left|\frac{3}{2},\frac{-1}{2}\right\rangle \\ \left|\frac{3}{2},\frac{-3}{2}\right\rangle \\ \left|\frac{1}{2},\frac{1}{2}\right\rangle \\ \left|\frac{1}{2},\frac{-1}{2}\right\rangle \end{matrix}$$

where

$$P = P_k + P_\varepsilon$$

$$Q = Q_k + Q_\varepsilon$$

$$R = R_k + R_\varepsilon$$

$$S = S_k + S_\varepsilon$$

$$P_k = (\frac{\hbar^2}{2m_0})\ \gamma_1\ (k_x{}^2 + k_y{}^2 + k_z{}^2)$$

$$Q_k = (\frac{\hbar^2}{2m_0})\ \gamma_2\ (k_x{}^2 + k_y{}^2 - 2k_z{}^2)$$

$$R_k = (\frac{\hbar^2}{2m_0})\ \sqrt{3}\ [-\gamma_2\ (k_x{}^2 - k_y{}^2) + 2i\gamma_3 k_x k_y]$$

$$S_k = (\frac{\hbar^2}{2m_0})\ 2\sqrt{3}\ \gamma_3\ (k_x - ik_y)k_z$$

$$P_\varepsilon = -a_v(\varepsilon_{xx} + \varepsilon_{yy} + \varepsilon_{zz})$$

$$Q_\varepsilon = -\frac{b}{2}(\varepsilon_{xx} + \varepsilon_{yy} - 2\varepsilon_{zz})$$

$$R_\varepsilon = -\frac{\sqrt{3}}{2}b(\varepsilon_{xx} - \varepsilon_{yy}) - id\varepsilon_{xy}$$

$$S_\varepsilon = -d(\varepsilon_{zx} - i\varepsilon_{yz})$$

where $\triangle$ is the spin-orbit splitting, γ_1, γ_2, and γ_3 are the Luttinger parameters, and a_v, b, and d are the Bir-Pikus deformation potentials. The basis function $|J, m_J>$ represents the Bloch wave function at the zone center. The parameters used in this thesis are listed in Table 2.1.

$$\left|\tfrac{3}{2}, \tfrac{3}{2}\right\rangle = \frac{-1}{\sqrt{2}}\left|(X + iY)\uparrow\right\rangle$$

$$\left|\tfrac{3}{2}, \tfrac{1}{2}\right\rangle = \frac{-1}{\sqrt{6}}\left|(X + iY)\downarrow\right\rangle + \sqrt{\frac{2}{3}}\left|Z\uparrow\right\rangle$$

$$\left|\tfrac{3}{2}, -\tfrac{1}{2}\right\rangle = \frac{1}{\sqrt{6}}\left|(X - iY)\uparrow\right\rangle + \sqrt{\frac{2}{3}}\left|Z\downarrow\right\rangle$$

$$\left|\tfrac{3}{2}, -\tfrac{3}{2}\right\rangle = \frac{1}{\sqrt{2}}\left|(X - iY)\downarrow\right\rangle$$

$$\left|\tfrac{1}{2}, \tfrac{1}{2}\right\rangle = \frac{1}{\sqrt{3}}\left|(X + iY)\downarrow\right\rangle + \frac{1}{\sqrt{3}}\left|Z\uparrow\right\rangle$$

$$\left|\tfrac{1}{2}, -\tfrac{1}{2}\right\rangle = \frac{1}{\sqrt{3}}\left|(X - iY)\uparrow\right\rangle - \frac{1}{\sqrt{3}}\left|Z\downarrow\right\rangle$$

2.2.2 Valence Band Structure of Bulk Si and Ge

Fig. 2.2 (a) and (b) shows the constant energy surface of the heavy-hole band for

Si and Ge, respectively. The constant energy is 100 meV below the zone center. As shown in the figure, the heavy-hole band depicts the twelve promising prongs and the energy anisotropy for Ge is less severe than that for Si.

2.3 Subband Structures in Infinite Quantum Wells

When an external voltage is applied in the z-direction, the Schrodinger equation under the Luttinger-Kohn model is [2.10, 2.11]

$$\left[H(k_x, k_y, k_z = -i\frac{\partial}{\partial z}) + qV(z)I_{6\times 6} \right] \varphi_{n,k_x,k_y}(z) = E_n(k_x, k_y) \cdot \varphi_{n,k_x,k_y}(z)$$

where $\varphi_{n,k_x,k_y}(z)$ is a 6x1 vector containing the components of the basis function, I_{6x6} is the identity matrix of order 6, V(z) is the quantum confinement energy caused by the external applied voltage, and E_n is the subband energy of the n-th subband. Since the system varies only along the z direction, and is translational invariant in the lateral directions. Then, we can express the Hamiltonian matrix element as a second-order polynomial in k_z and replace the wave vector-component k_z by the operator $k_z = -i\partial/\partial z$ [2.12].

$$H_{ij} = H_{ij}^{(2)} \cdot k_z^2 + H_{ij}^{(1)}(k_{\|}) \cdot k_z + H_{ij}^{(0)}(k_{\|})$$

$$[-H^{(2)}\frac{\partial^2}{\partial z^2} - iH^{(1)}\frac{\partial}{\partial z} + H^{(0)} + qV(z)] \cdot \varphi_{n,k_x,k_y}(z) = E_n(k_x, k_y) \cdot \varphi_{n,k_x,k_y}(z)$$

Fig. 2.3 (a) and (b) show the comparison of hole subband structures calculated with the Luttinger-Kohn model and bond-orbital model for a 30 Å (001) infinite Si and Ge quantum wells, respectively. Energy is plotted along wave-vector direction of

<100> and <110> and confinement direction is taken to be along the z direction. Two points are worth noting. First, the Luttinger-Kohn model can yield reliable results only near the valence band maxima, and it's not appropriate for the high energy portion of a valence band. Second, Ge generally has small quantization masses compared to that of Si, resulting in larger energy separations. For instance, as shown in Fig. 2.3 (b), an energy separation of 0.1 eV between the first and second subband is obtained.

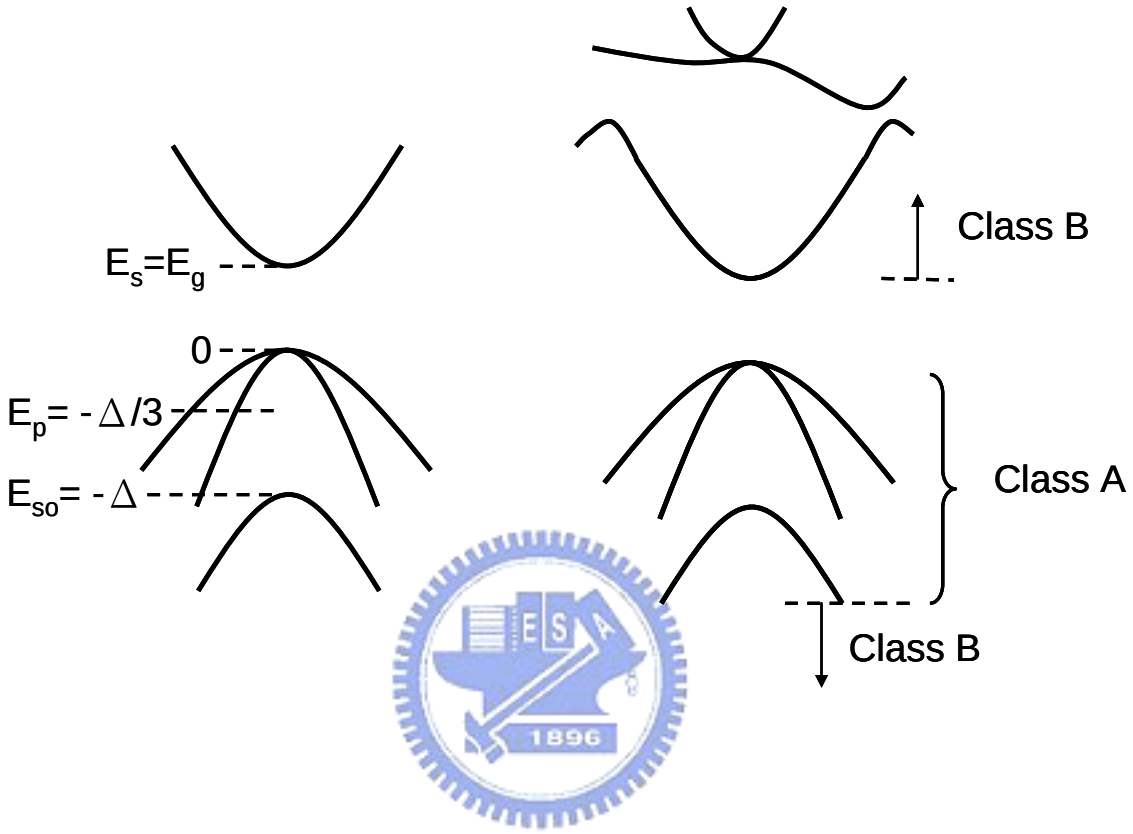

Fig. 2.1 (a) The kp method in Kane's model. (b) The Luttinger-Kohn model.

Table 2.1 Material parameters for Si and Ge, respectively.

Material Parameters	Symbol	Unit	Si	Ref.	Ge	Ref.
Valence band structure	γ_1		4.285	[2.8]	13.38	[2.8]
	γ_2		0.339	[2.8]	4.24	[2.8]
	γ_3		1.446	[2.8]	5.69	[2.8]
Spin-orbit splitting	Δ	eV	0.044	[2.8]	0.297	[2.8]
Deformation potential	a	eV	2.05	[2.9]	2.0	[2.9]
	b	eV	-2.1	[2.9]	-2.2	[2.9]
	d	eV	-4.85	[2.9]	-4.4	[2.9]
Lattice constant	a_0		5.431		5.646	
Dielectric constant	ε		11.7		16.0	
Elastic constant	c_{11}	10^{11}dyn/cm^2	16.577	[2.9]	12.853	[2.9]
	c_{12}	10^{11}dyn/cm^2	6.393	[2.9]	4.826	[2.9]
	c_{44}	10^{11}dyn/cm^2	7.962	[2.9]	6.680	[2.9]

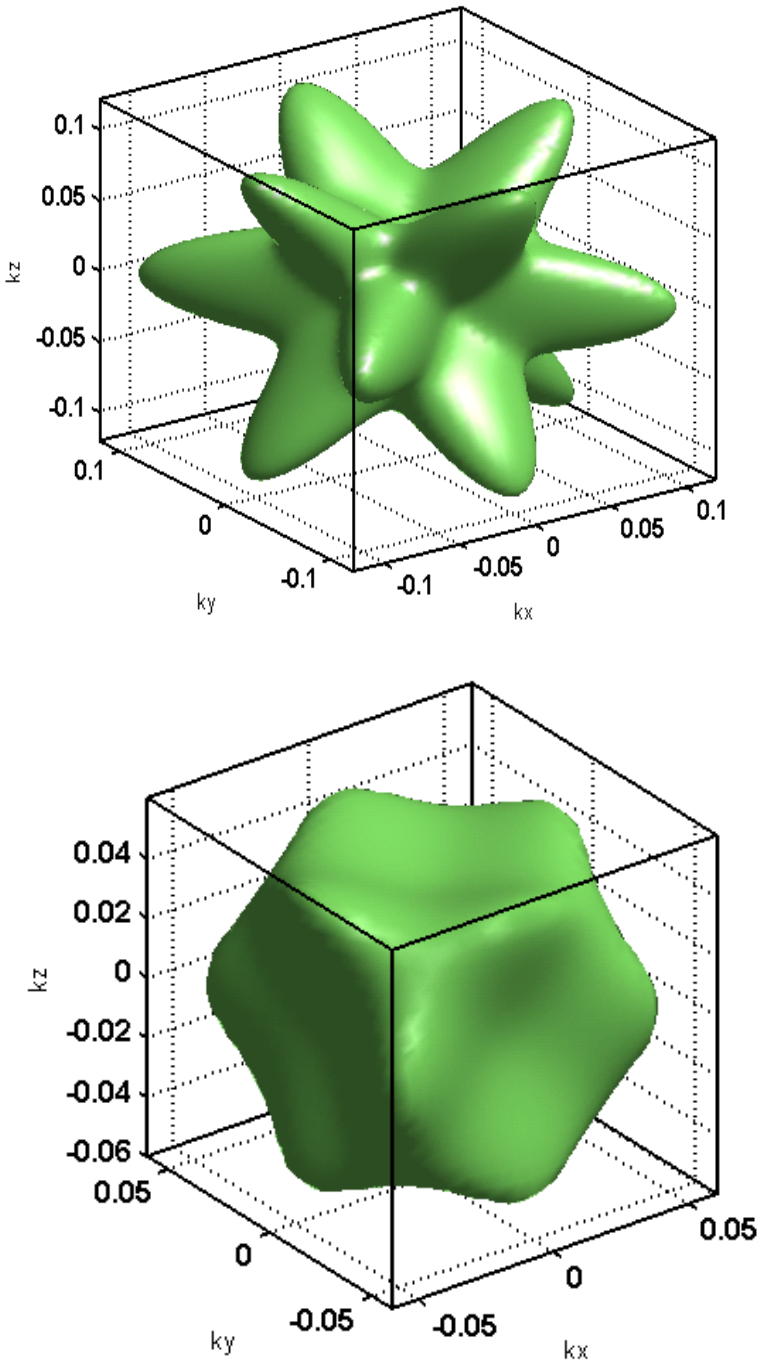

Fig. 2.2 Constant energy surfaces of the heavy-hole hand for (a) Si and (b) Ge with energy 100meV below the zone center.

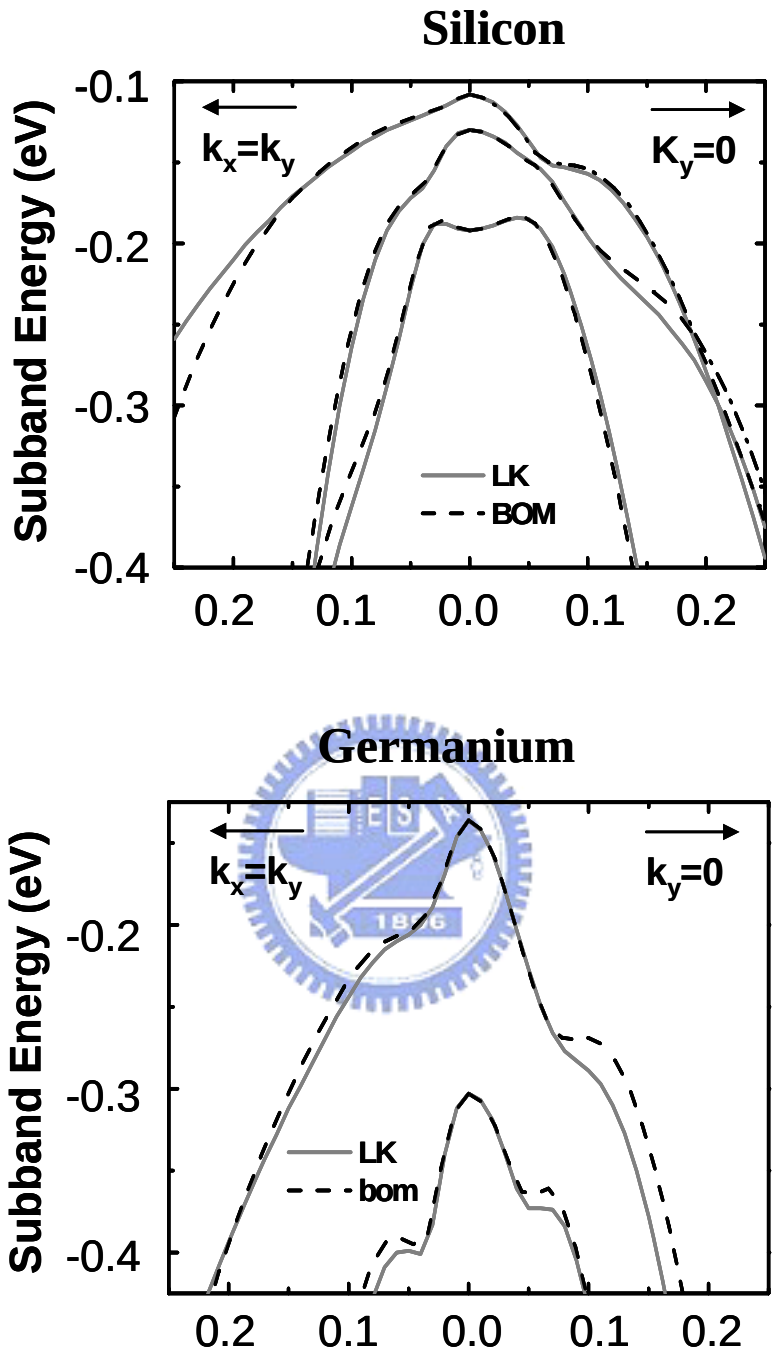

Fig. 2.3 Hole subband structure for a 30-Å (001) infinite Si and Ge quantum well. Calculation from the Luttinger-Kohn model is compared with that from the bond-orbital model. Energy plotted along wave-vector direction of <100> and <110>. Confinement direction is taken to be along *z* direction.

Chapter 3

Valence Band Calculation in Silicon Inversion Layer by a Self-consistent Approach

3.1 Introduction

The effective mass approximation has been widely applied to the electron quantization in silicon inversion layer. Although such a treatment has also been used for the hole case [3.1,3.2], this methodology will result in an incorrect valence subband structures due to the band-mixing of the heavy, light and split-off bands and thus lead to an incorrect carrier transport behavior. One of the methods to incorporate these effects is based on the diagonalization of the Luttinger-Kohn Hamiltonian in the framework of the effective mass theory [2.12, 2.13]. The strain effect can be easily incorporated into Luttinger-Kohn Hamiltonian by including the Bir-Pikus deformation potentials.

3.2 Device Configuration and Simulation Technique

Fig. 3.1 shows the simulated one-dimensional (1D) Si–SiO_2 pMOS structure on a 500nm (100) silicon substrate. The coupled Schrödinger and Poisson equation is solved by using the three-point finite difference method with a nonuniform mesh. 100 grid points for a 500 nm substrate are used to obtain well converged wavefunctions and subband energies. Furthermore, the linear 1D Poisson equation is solved by the Newton iteration scheme.

3.2.1 Formulation for the Schrödinger Equation

The formulation for the Schrödinger Equation had been described in chapter 2 and the corresponding equations are described as follows

$$\left[H(k_x, k_y, k_z = -i\frac{\partial}{\partial z}) + qV(z)I_{6\times 6} \right] \varphi_{n,k_x,k_y}(z) = E_n(k_x, k_y) \cdot \varphi_{n,k_x,k_y}(z) \qquad (1)$$

$$H_{ij} = H_{ij}^{(2)} \cdot k_z^2 + H_{ij}^{(1)}(k_{\|}) \cdot k_z + H_{ij}^{(0)}(k_{\|}) \qquad (2)$$

$$[-H^{(2)}\frac{\partial^2}{\partial z^2} - iH^{(1)}\frac{\partial}{\partial z} + H^{(0)} + qV(z)] \cdot \varphi_{n,k_x,k_y}(z) = E_n(k_x, k_y) \cdot \varphi_{n,k_x,k_y}(z) \qquad (3)$$

In this section, we mainly focus on the formulation of the Schrödinger Equation with a nonuniform mesh. Following by the approach given in [3.3], we firstly discretized the differential equation by using a three-point finite difference method. The index *i* represents each discretized lattice point and h_i stands for the mesh size between adjacent grid points x_i and x_{i+1}. This will give an asymmetric tridiagonal-block matrix if the mesh spacings are nonuniform, as shown in Fig. 3.2 (a), which yields a $6N_z$ x $6N_z$ eigenvalue problem.

$$\begin{aligned} H_{i,i} &= H^{(2)}(\frac{1}{h_{i-1}} + \frac{1}{h_i}) \cdot (\frac{2}{h_{i-1} + h_i}) + H^{(0)} + V(z) \\ H_{i,i-1} &= -H^{(2)}(\frac{1}{h_{i-1}}) \cdot (\frac{2}{h_{i-1} + h_i}) + \frac{iH^{(1)}}{2} \cdot (\frac{2}{h_{i-1} + h_i}) \\ H_{i,i+1} &= -H^{(2)}(\frac{1}{h_i}) \cdot (\frac{2}{h_{i-1} + h_i}) - \frac{iH^{(1)}}{2} \cdot (\frac{2}{h_{i-1} + h_i}) \end{aligned} \qquad (4)$$

This may be cast in the form of a matrix equation,

$$H\varphi = \lambda\varphi \qquad (5)$$

Here, we define the following parameters:

$$L_i^2 = (h_i + h_{i-1})/2 \quad (6)$$

Thus, the matrix becomes

$$\begin{aligned} B'_{i,i} &= \{H^{(2)}(\frac{1}{h_{i-1}} + \frac{1}{h_i}) + (H^{(0)} + V(z)) \cdot (\frac{h_{i-1} + h_i}{2})\} \\ B'_{i,i-1} &= \{-H^{(2)}(\frac{1}{h_{i-1}}) + \frac{iH^{(1)}}{2}\} \\ B'_{i,i+1} &= \{-H^{(2)}(\frac{1}{h_i}) - \frac{iH^{(1)}}{2}\} \end{aligned} \quad (7)$$

We set $B_{ij} = L_i^2 H_{ij}$

Then it can be easily shown that instead of solving Eq. (5), one can solve Eq. (8) to obtain the eigenvalue λ corresponding to the eigenfunction Φ due to the symmetric and tridiagonal matrix A, which ensures the real-valued eigenvalues.

$$A\Phi = \lambda\Phi \quad (8)$$

where $A = L^{-1}BL^{-1}$ and $\varphi = L^{-1}\Phi$

3.2.2 Formulation for the Poisson Equation

The one dimensional Poisson equation taking position dependence of dielectric constant into consideration is expressed as

$$\nabla \cdot (\varepsilon(z) \cdot \nabla\phi(z)) = -q \cdot (p(z) - n(z) - N_A^-(z) + N_D^+(z)) \quad (9)$$

Where q represents elementary charge equal to $1.6\text{x}10^{-19}$ coulomb, ε(z) is the position-dependent dielectric constant in each material, and $\phi(z)$ is the electrostatic potential. In the simulation, complete ionization at 300K is assumed. In oxide region, Eq. (9) reduces to

$$\nabla^2\phi(z) = 0 \qquad (10)$$

Discretization of Eq. (10) is given by

$$\phi_i = \frac{1}{\Delta}\left(\frac{1}{x_i}\phi_{i+1} + \frac{1}{x_{i-1}}\phi_{i-1}\right)$$

where $\Delta = \left(\frac{1}{x_i} + \frac{1}{x_{i-1}}\right)$ and x_i and x_{i+1} are defined in Fig. 3.2 (b).

In semiconductor region, discretization of Eq. (9) can be obtained first by linearizing Eq. (9), i.e. let $\phi^{(k+1)} = \phi^{(k)} + \delta$, then

$$\varepsilon\,\nabla\cdot\nabla\delta - q\beta(n+p)\cdot\delta = q(n - p + N_A - N_D) - \varepsilon\,\nabla\cdot\nabla\phi^{(k)} \qquad (11)$$

where $\beta = q/kT$

Appling three-point finite difference method gives

$$\varepsilon_1\frac{\frac{\delta_{i+1}-\delta_i}{x_i} - \frac{\delta_i-\delta_{i-1}}{x_{i-1}}}{\frac{1}{2}(x_i + x_{i-1})} - q\beta(n+p)\delta_i = q(n - p + N_A - N_D) - \varepsilon_1\frac{\frac{\phi_{i+1}-\phi_i}{x_i} - \frac{\phi_i-\phi_{i-1}}{x_{i-1}}}{\frac{1}{2}(x_i + x_{i-1})} \qquad (12)$$

or $b_{i-1}\delta_{i-1} + \delta_i + a_{i+1}\delta_{i+1} = c_i$

3.2.3 Flow Chart of Self-consistent Calculation

The simulation flow of the coupled self-consistent Schrödinger and the Poisson equation is shown in Fig. 3.3. First, we obtained the classical electrostatic potential distribution by solving the Poisson equation. Then, we get the corresponding subbands and wavefunctions by solving the Schrödinger equation according to Eq. (8). Here, we have defined an energy, E_{lim}, to obtain the hole concentrations in the continuum (p_{3d}) and in the subbands (p_{2d}). For energies below E_{lim} the hole concentration (p_{3d}) is evaluated as an incomplete Fermi integral [3.4] by using a continuous distribution of the density of states. For energies above E_{lim}, the subband energies are calculated and the two-dimensional hole concentration is calculated by Eq. (13) [3.4].

$$p_{2d}(z) = \sum_{i,j} \frac{m^* kT}{\pi\hbar^2} \cdot \ln(1+\exp(\frac{E_i - E_{Fp}}{kT})) \left|\varphi_j(z)\right|^2 \qquad (13)$$

With the new $\phi(z)$, and using Eq. (3) and (9), we calculate $p(z)$ once again, and continue iteratively until convergence is obtained. For a particular gate bias, this method allows us to obtain the band structure in the k_x-k_y plane, the distribution of the potential due to the external voltage along the z direction of the device, and the two-dimensional hole concentration in each subband.

3.3 Simulation Results

The simulated structure is shown in Fig. 3.1, where we have depicted the potential distribution of pMOS. The applied bias, V_g-V_{fb}, is changed from -1.5 to 4.0 V. The doping of the n-type substrate is $5\text{x}10^{17}$ cm^{-3}. The 6nm oxide layer is used to assume no direct tunneling current.

Fig. 3.4 and Fig. 3.5 illustrates the components of the wavefunction for each subband and valence band structure on (001) Si substrate with applied bias V_g-V_{fb}= -3.0(V) at Γ point k=[0,0], respectively. Each subband is composed of six basis functions, $|\frac{3}{2},\pm\frac{3}{2}>$ (heavy hole states), $|\frac{3}{2},\pm\frac{1}{2}>$ (light hole states), and $|\frac{1}{2},\pm\frac{1}{2}>$ (split-off states). The labels of the subbands are defined from the characteristic basis states at the zone center. For example, HH1 denotes the first heavy-hole subband, in which the two heavy-hole basis functions $|\frac{3}{2},\pm\frac{3}{2}>$ are dominant. Likewise, LH1 is the first light-hole subband, SO1 is the first split-off subband. Fig. 3.6 shows the subband energies as a function of the surface field on (001) Si substrate. Note that the heavy hole-like subband is the ground state. The calculated subband structures along two principal directions, $[k_x,k_y]$=[k,0] and [k,k], are also plotted in Fig. 3.7. Fig. 3.8 demonstrates the wavefunction percentage of the HH1 subband along $[k_x,k_y]$=[k,0.5k]. The characteristic of the subband becomes mixed as the $k_{//}$ is separated from zero. From Fig. 3.7 and Fig. 3.8, it should be noted that the intersubband transition energy is strongly affected by the band-mixing effect.

Fig. 3.9 shows constant energy contours represented by the polar coordinates for the subbands HH1, LH1 and SO1. The strong band-mixing effect results in a warping of the constant energy contour. The constant energy contours for the HH1, LH1 and SO1 subbands are illustrated in Fig. 3.10 and the constant energy lines are separated by 25meV. Apparently, the effective mass varies in different directions. For this reason, an analytical form is inadequate and the numerical tabular form for the subband structure is needed to perform the Monte Carlo simulation. Fig 3.11 (a) and (b) shows the constant energy contours of various subbands on (001) and (110) Si substrate, respectively. It can be seen clearly that the density of states of (110) Si substrate is smaller that that of (001) Si substrate due to smaller available *k* states

between E and $E+\triangle E$. Furthermore, Fig. 3.12 shows the calculated density of states as a function of energy on (001) and (110) Si substrate according to [3.5]

$$D(E) = \frac{2}{(2\pi)^2} \int_0^{2\pi} \frac{k}{|\nabla_k E|} d\theta$$

Lower density of states on (110) substrate compared to that on (001) suggests that the implementation of (110) substrate for the device's active layer will be useful in achieving a high mobility channel [3.6].

Fig. 13 shows the two-dimensional hole concentration distribution for different gate bias for a 6nm oxide thickness. Apparently, the peak of the hole concentration is decreased as the gate bias is decreased. On the other hand, the distance corresponding to the peak hole concentration is shorter with larger gate bias. The inversion hole density is also shown in Fig. 14. Fig. 15 shows the behavior of inversion layer centroid, Z_{avg}, as a function of gate bias, where Z_{avg} is defined as

$$Z_{avg} = \frac{\int_{Si} p(z) \cdot z \cdot dz}{\int_{Si} p(z) \cdot dz} \qquad (14)$$

Our simulation has obtained a Z_{avg} between 2.48nm and 1.84 nm for V_g-V_{fb}= -1.5 and -4 V, respectively. Z_{avg} has been shown to be an important parameter in electron modeling [3.7] and it is also expected to be similar in the hole confinement. Moreover, to assess the importance of several scattering mechanisms as interface roughness and coulomb scattering, precise calculations of Z_{avg} are needed to determine the distance from the interface where carriers concentrate, which will be shown in chapter 4. It's noted that Z_{avg} is dependent on substrate doping, oxide thickness, bias and so on.

Finally, we compared the hole concentration distributions on (001) and (110) Si substrate with same applied gate bias. Fig. 16 shows that the peak depth of the hole concentration on (110) Si substrate is closer to SiO_2/Si interface than on (001) Si, which implies clear difference in (110) and (001) inversion layer thickness. It can be easily realized from the fact that for the bulk Si band structure, (110) surface yields a larger quantization mass, which will suffer larger confinement effect. As a result, a larger confinement effect results in smaller Z_{avg}, which leads to smaller inversion layer thickness. The comparison of Z_{avg} on (001) and (110) Si substrate is also shown in Fig. 17. The calculated Z_{avg} on (110) is 1nm thinner than that on (001) for V_g-V_{fb}= -3.0 V, which implies that in terms of inversion layer capacitance, the (110) pFETs show higher performance than (001) pFETs [3.8].

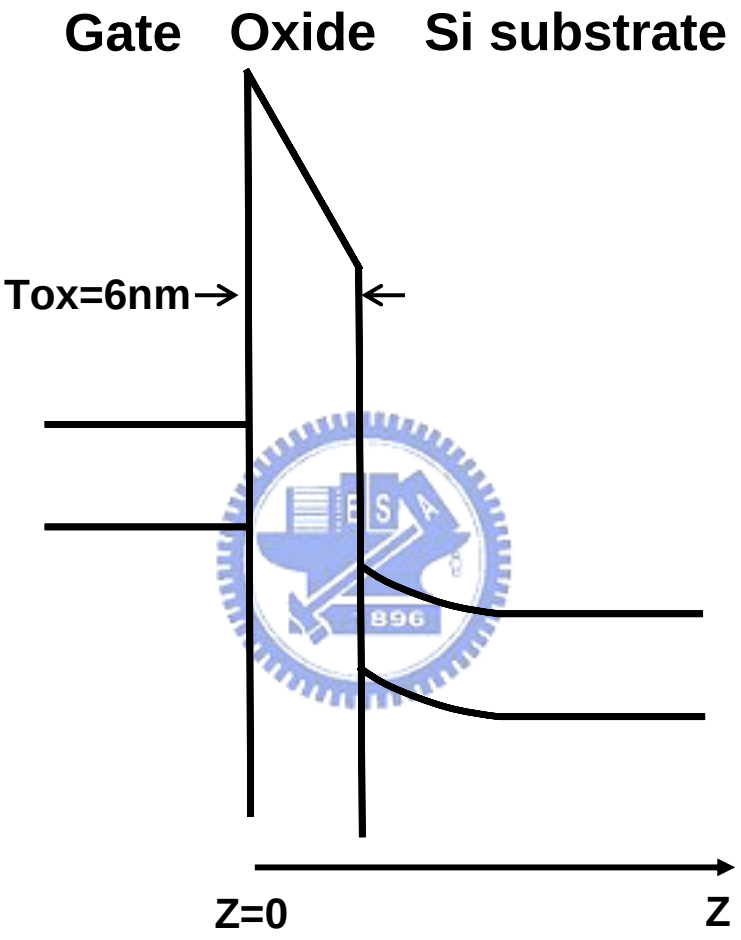

Fig. 3.1 Schematics of the band energy of the structure.

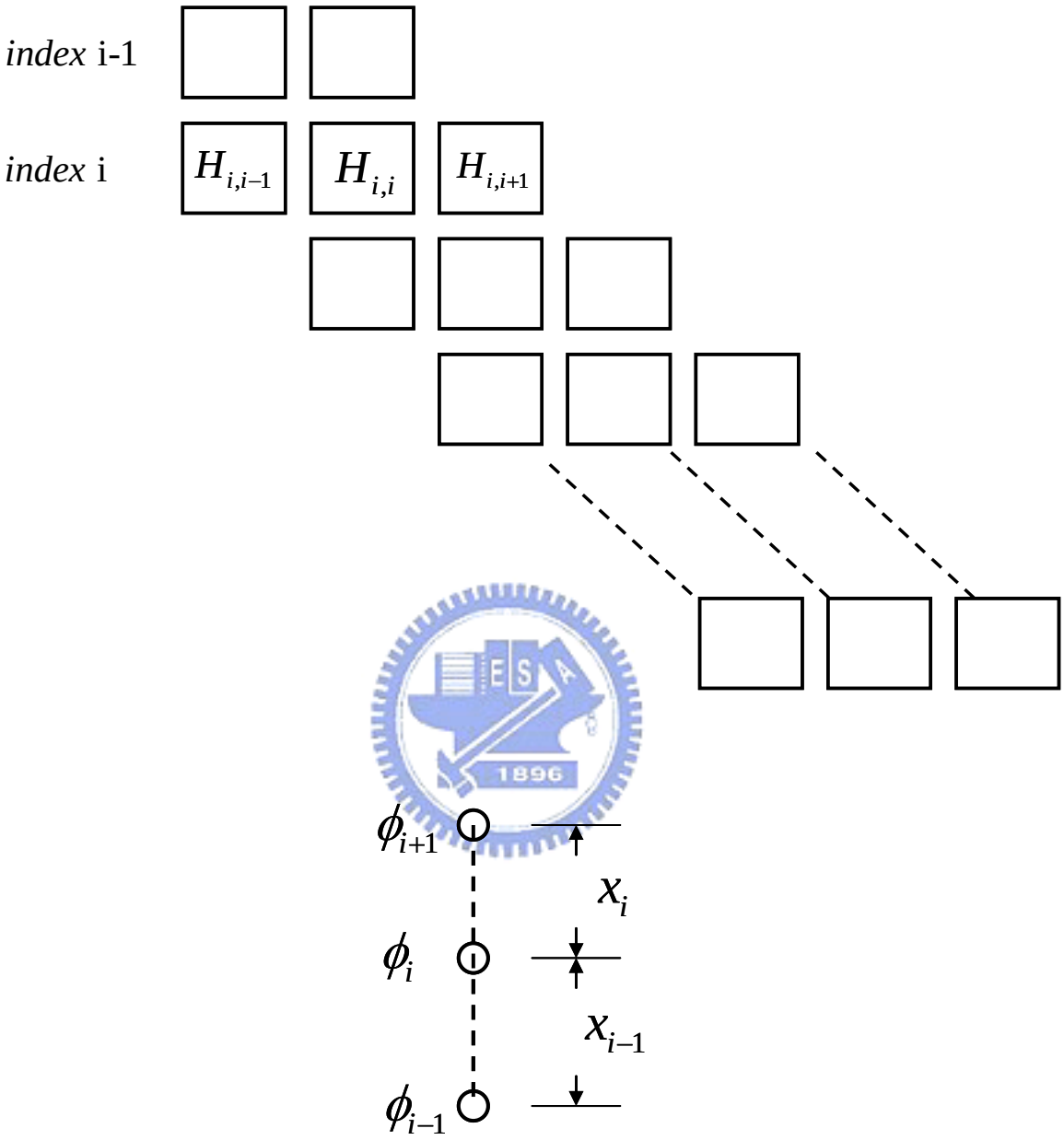

Fig. 3.2 (a) Tridiagonal block matrix for the Schrodinger equation. (b) Discretization of the potential using a nonuniform mesh.

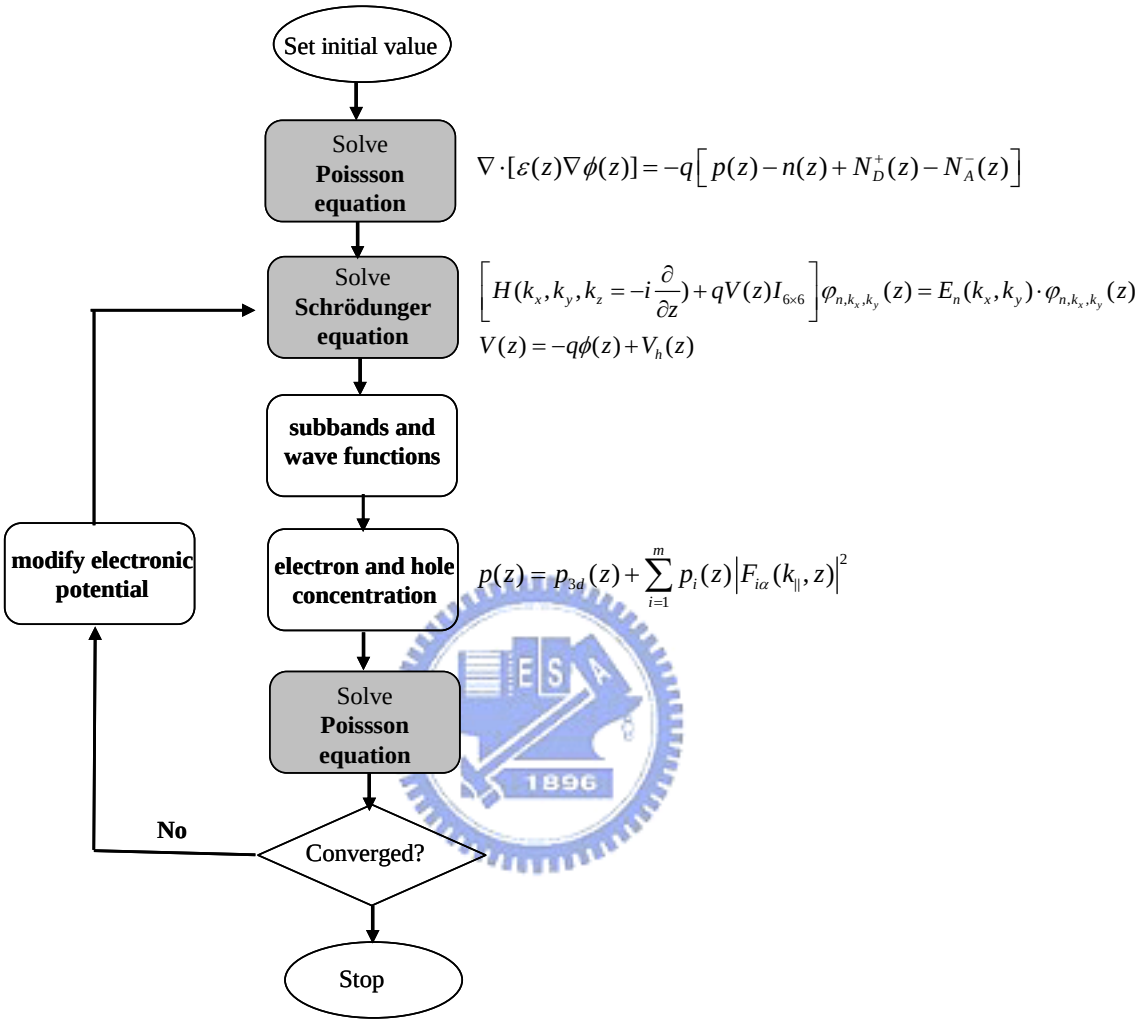

Fig. 3.3 Flowchart of self-consistent calculation by solving the Schrödinger and the Poisson equations.

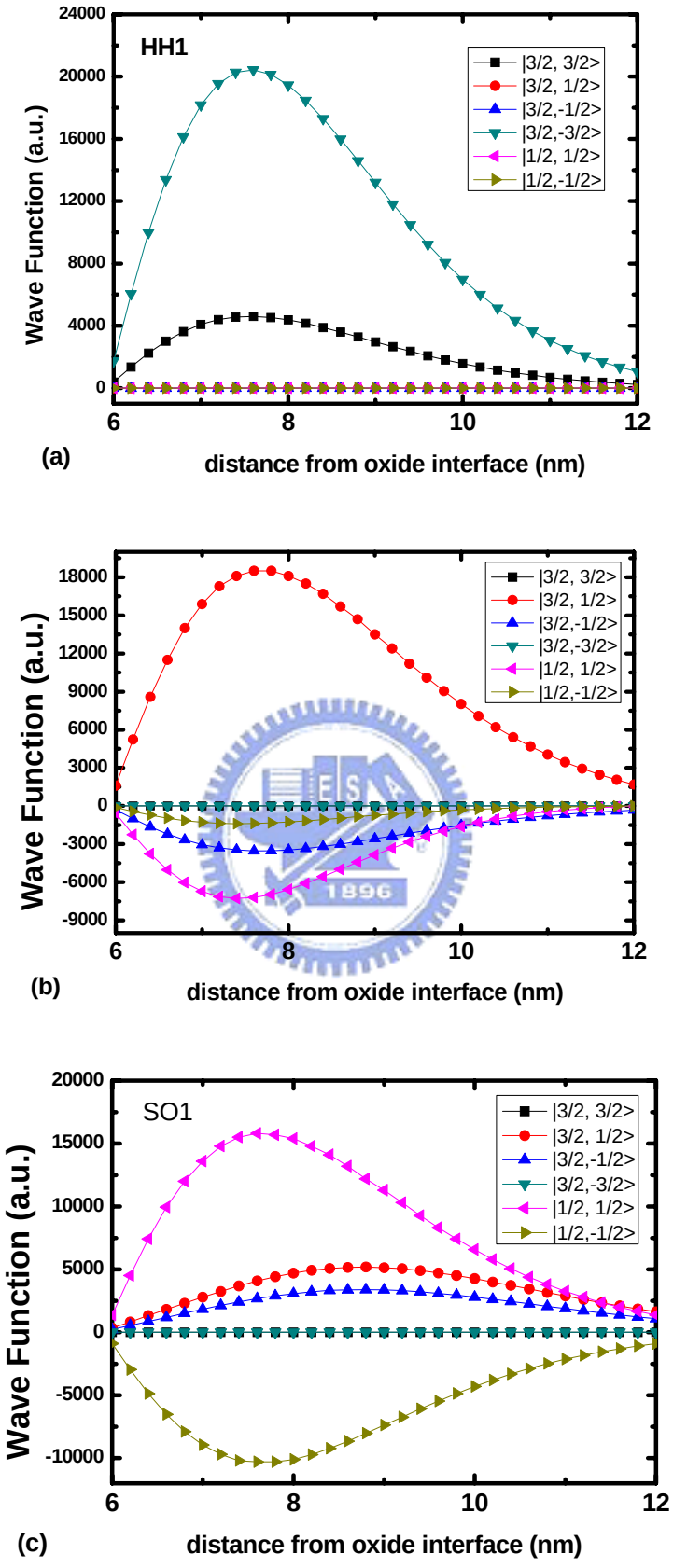

Fig. 3.4 The components of the wave function at zone center for (a) HH1, (b) LH1, and (c) SO1.

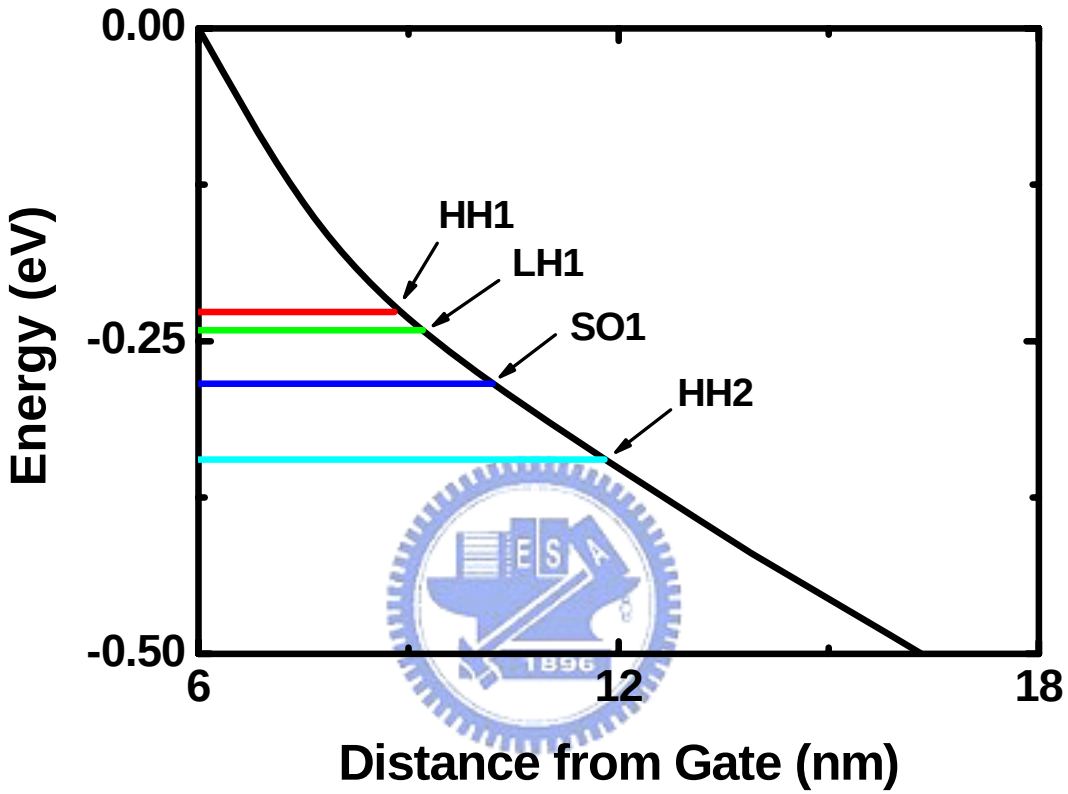

Fig. 3.5 The calculated valence band structure on (001) Si substrate. The V_g-V_{fb}= -3.0V. The n-type substrate doping is $5*10^{17}$ cm^{-3}.

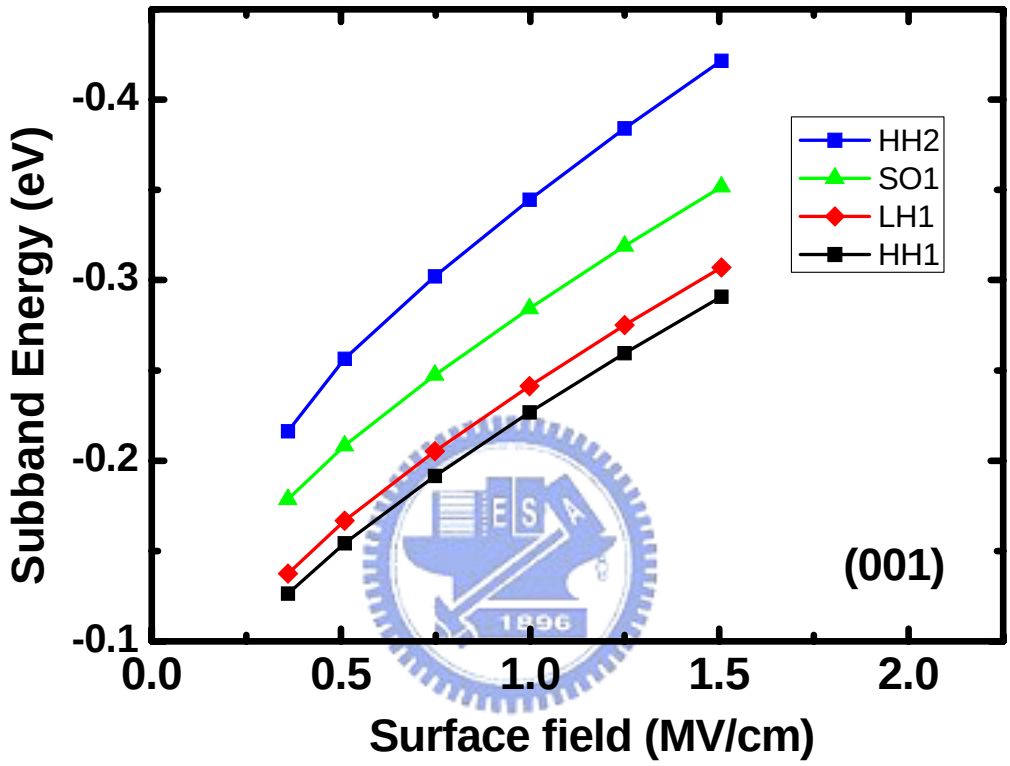

Fig. 3.6 The energies of the subbands as a function of the surface field on (001) Si substrate.

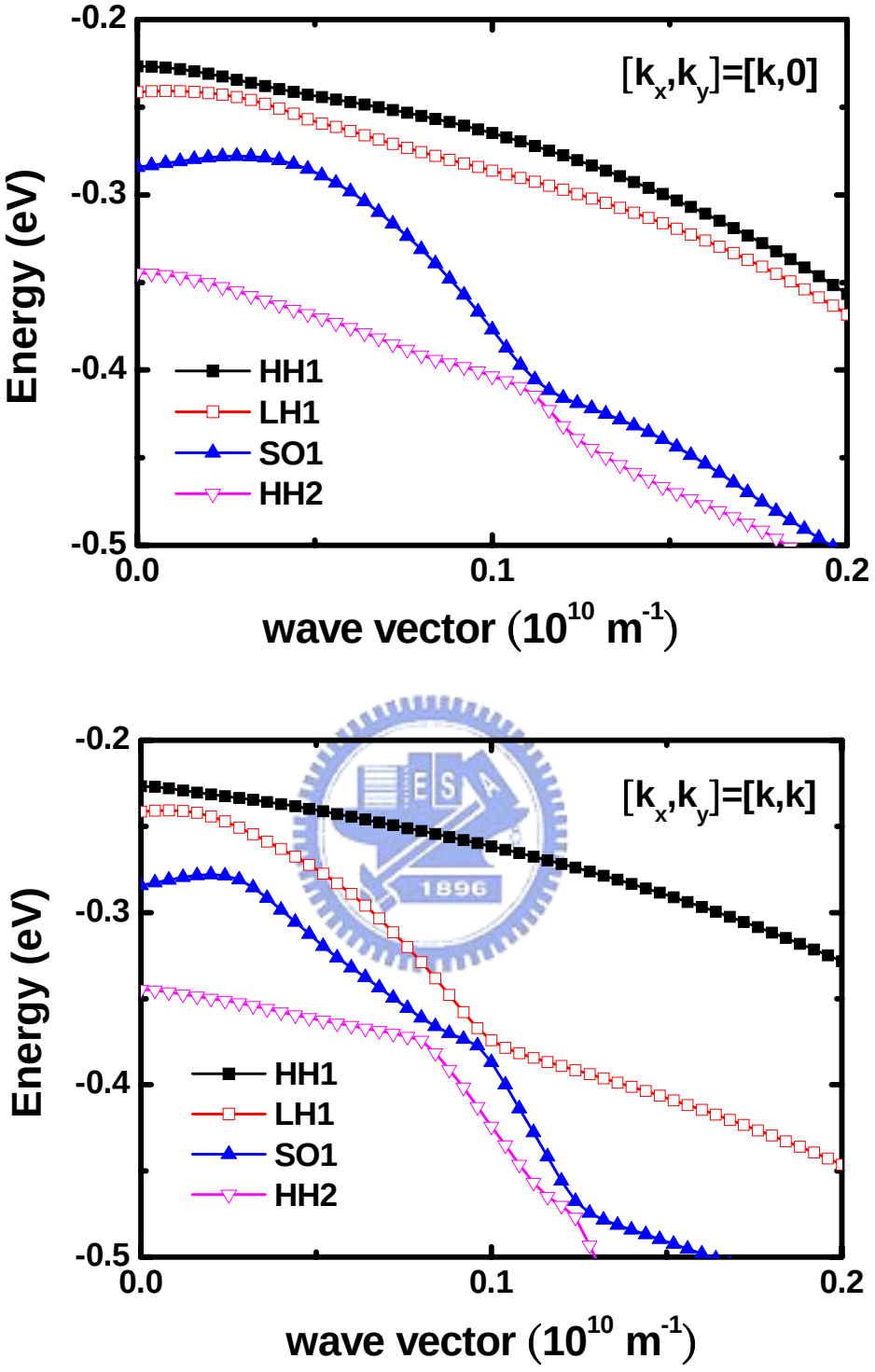

Fig. 3.7 The subband structures along two principal directions for 2D holes on (001) Si substrate at V_g-V_{fb}=-3.0V.

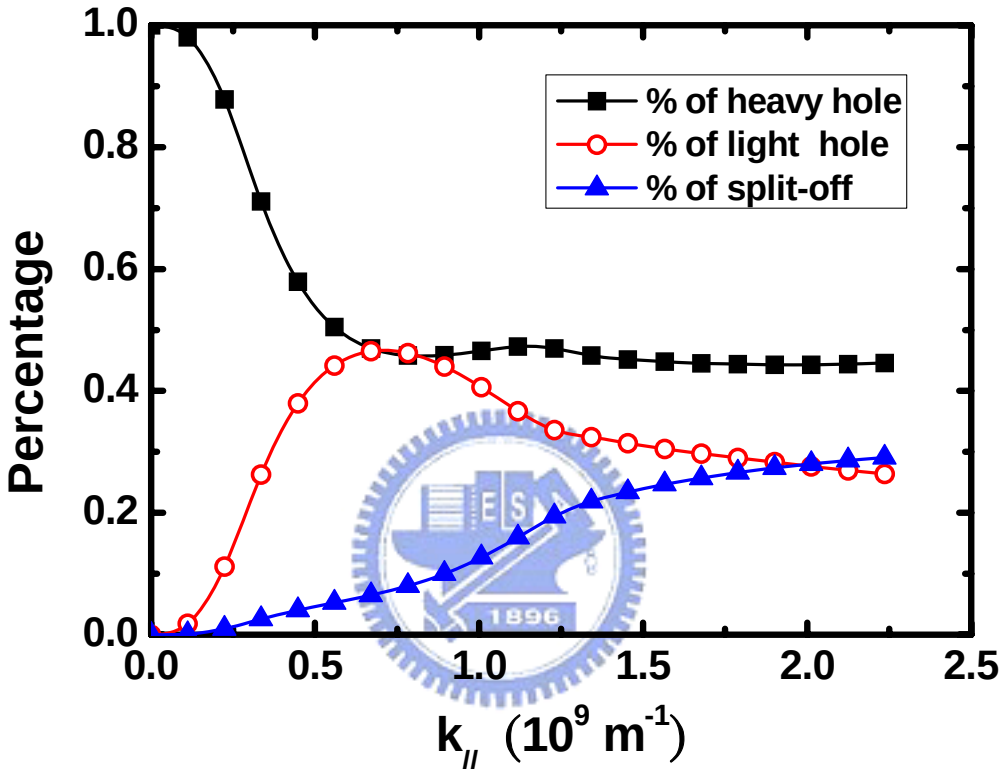

Fig. 3.8 Nature of the 1st subband on (001) Si substrate. The wave-vector is along $[k_x, k_y]=[k, 0.5k]$ at $V_g-V_{fb}=-3.0V$.

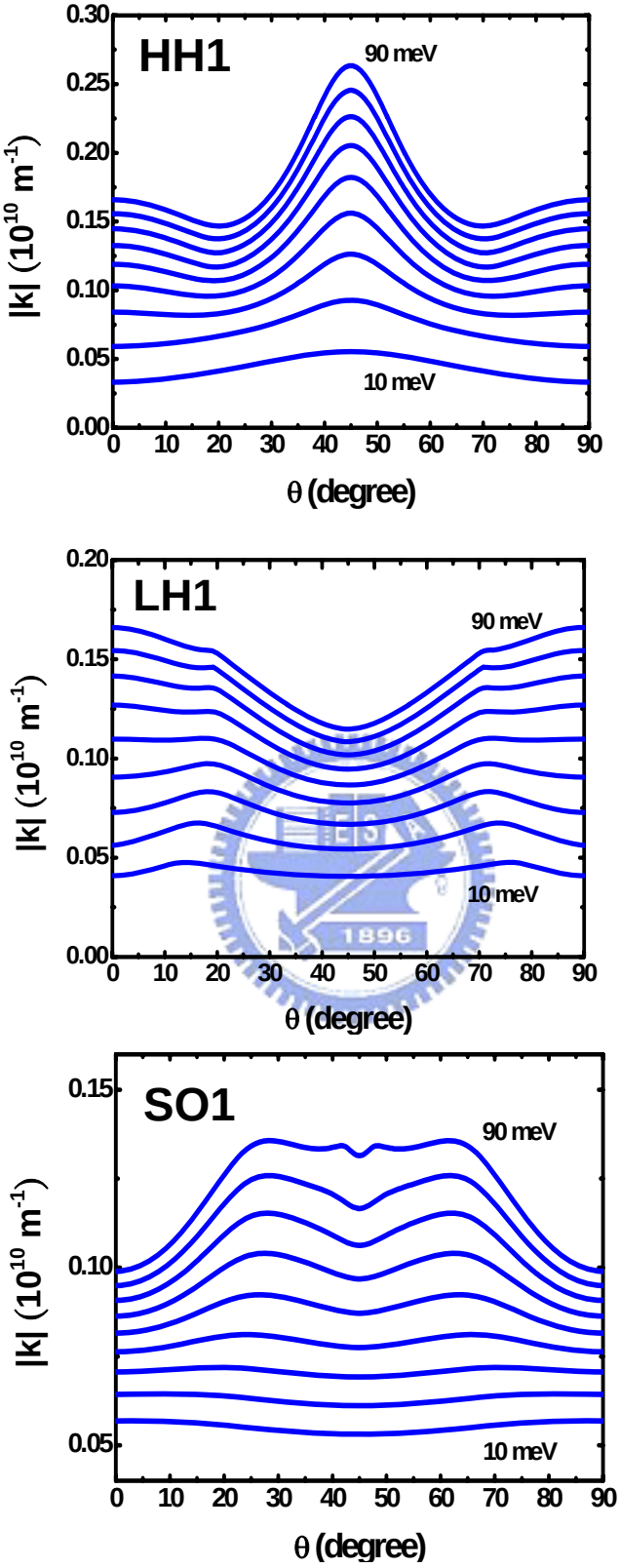

Fig. 3.9 The constant energy contours in a polar coordinate representation for the subbands HH1, LH1, and SO1.

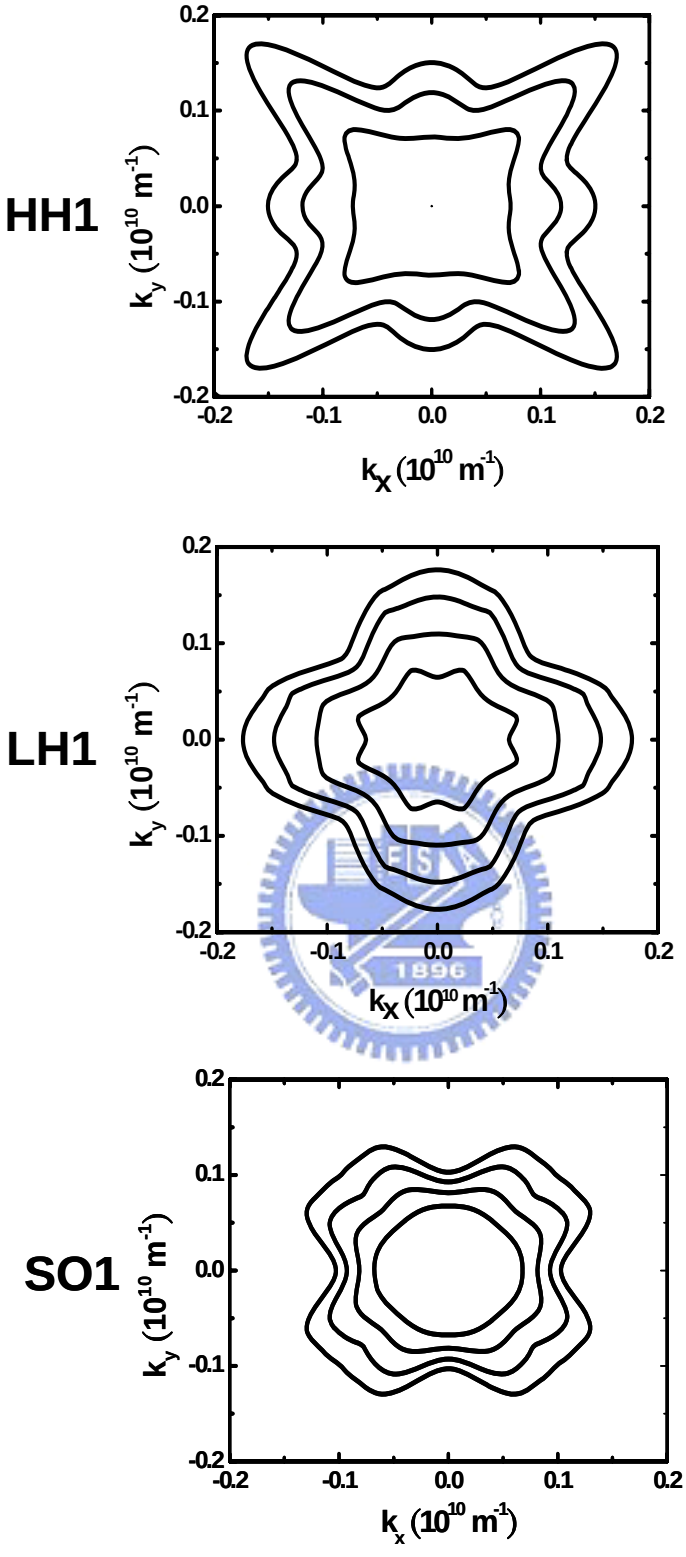

Fig. 3.10 Constant energy contours of the HH1, LH1 and SO1 band. The constant energy lines are separated by 25meV at V_g-V_{fb}=-3.0V.

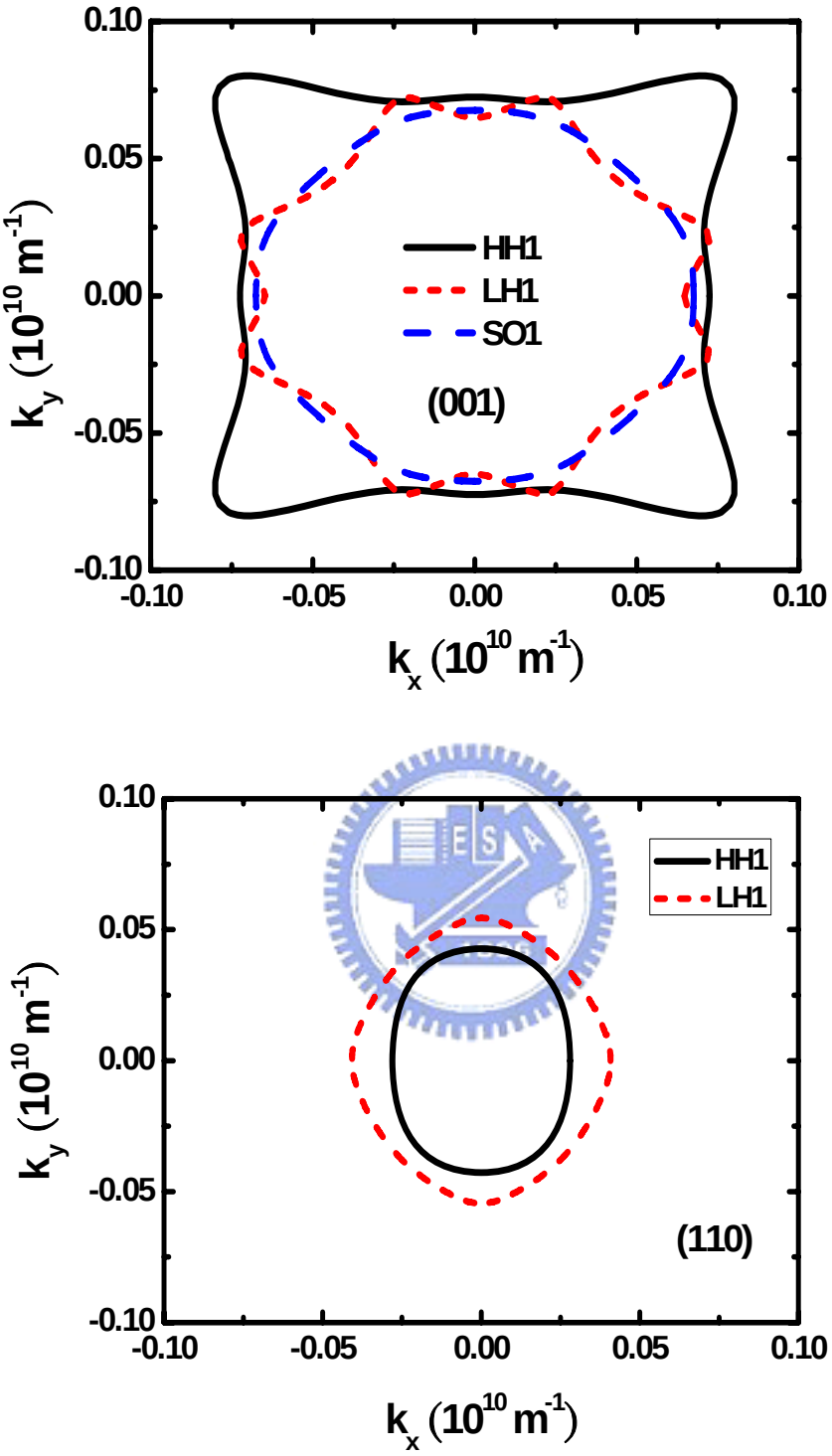

Fig. 3.11 Constant energy contours of the HH1, LH1 and SO1 subbands for (a) (001) and (b) (110) substrate at V_g-V_{fb}=-3.0V. The constant energy lines is 25meV. Only one spin state is plotted for clarity.

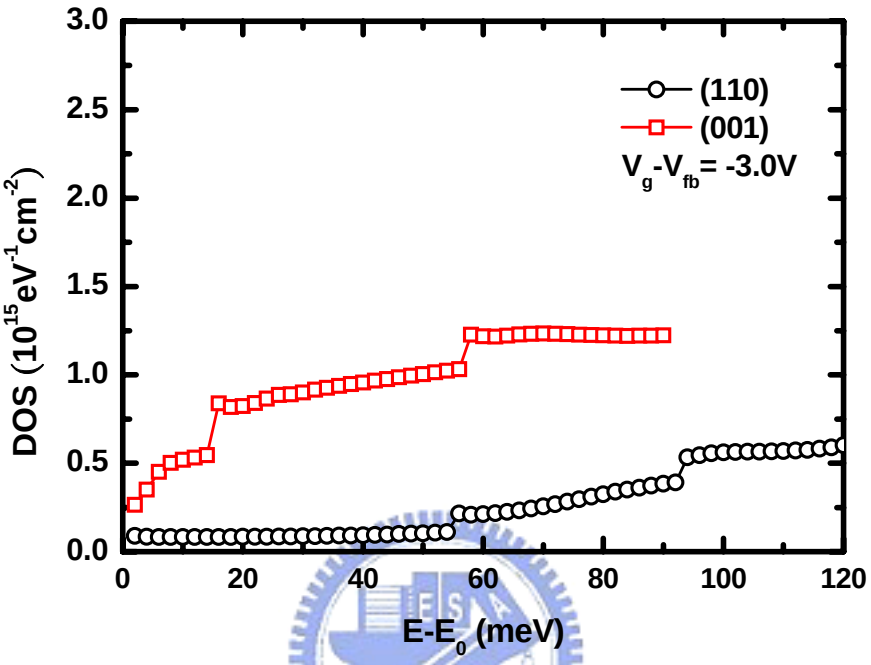

Fig. 3.12 Density-of-states of Si (001) and (110) substrates. E_0 is the minimum of the lowest subband.

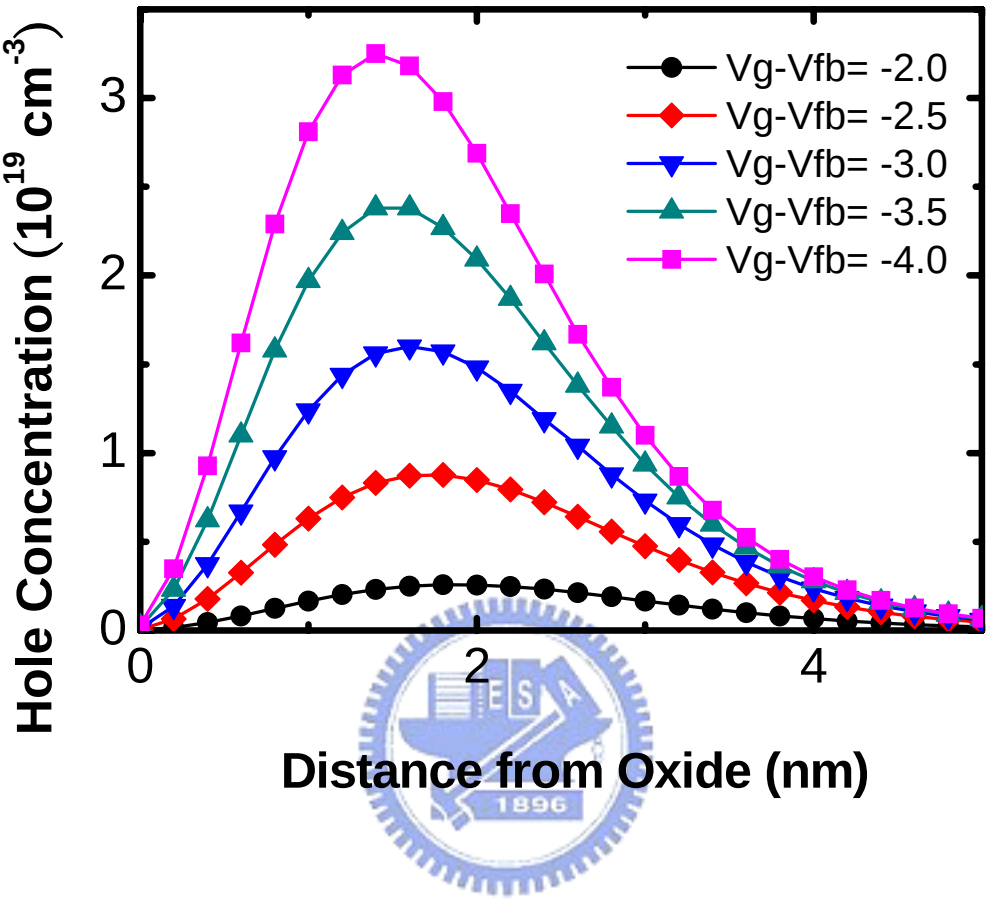

Fig. 3.13 The hole concentration distribution for different gate bias.

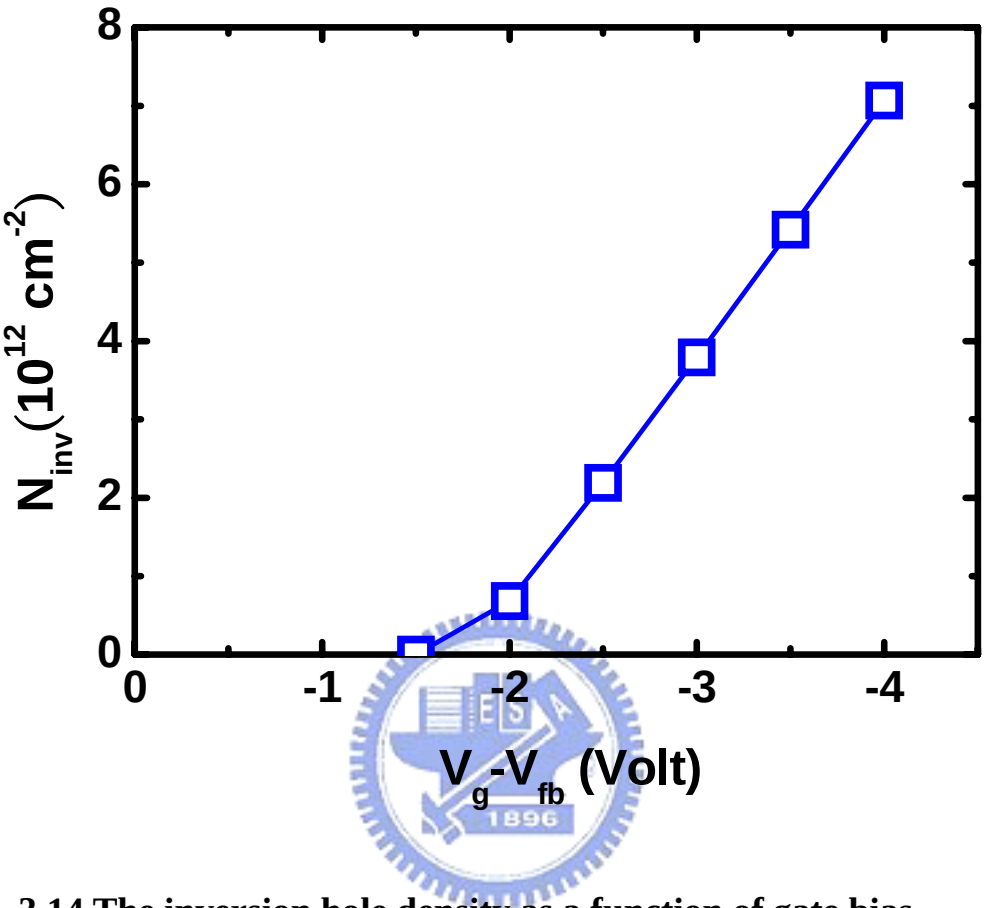

Fig. 3.14 The inversion hole density as a function of gate bias.

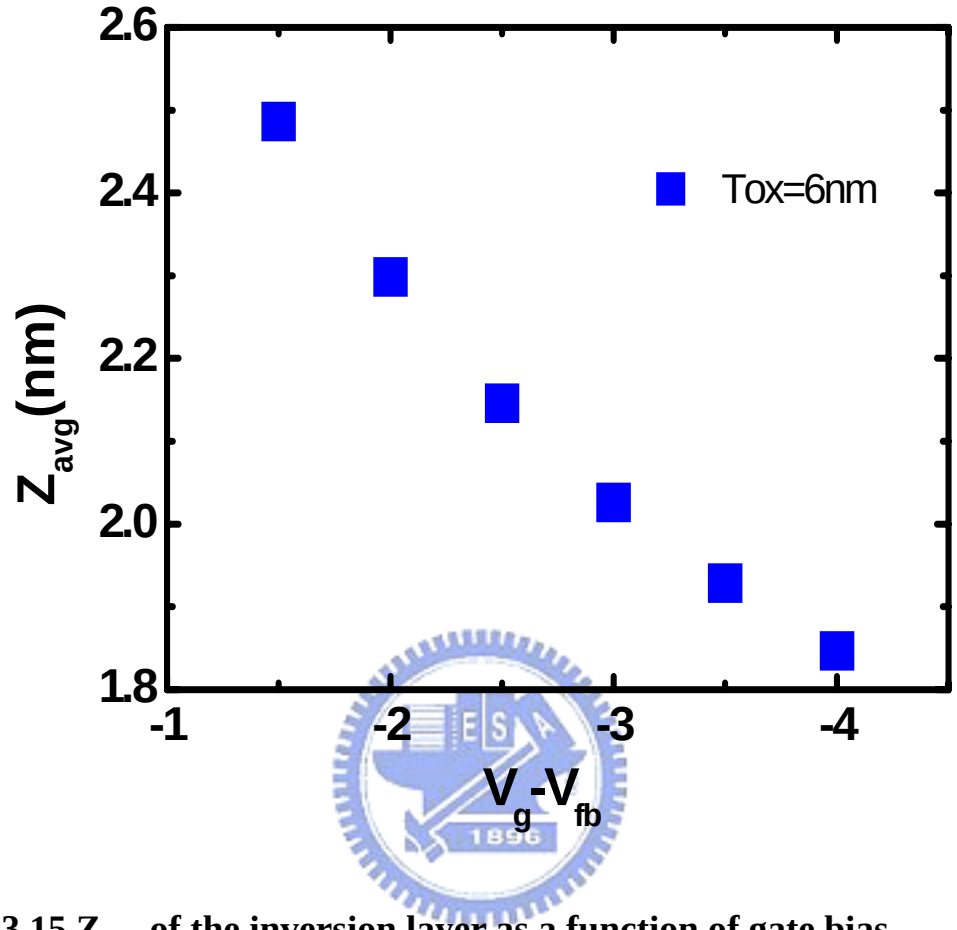

Fig. 3.15 Z_{avg} of the inversion layer as a function of gate bias.

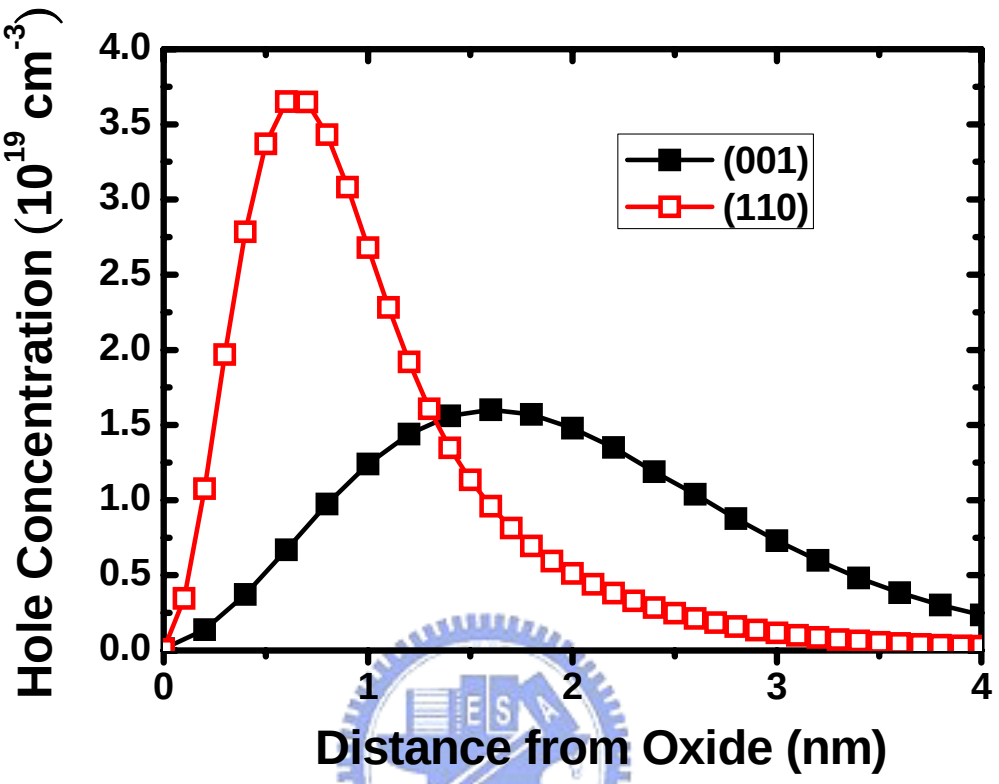

Fig. 3.16 The hole concentration distributions on (001) and (110) Si substrates at V_g-V_{fb}=-3.0V.

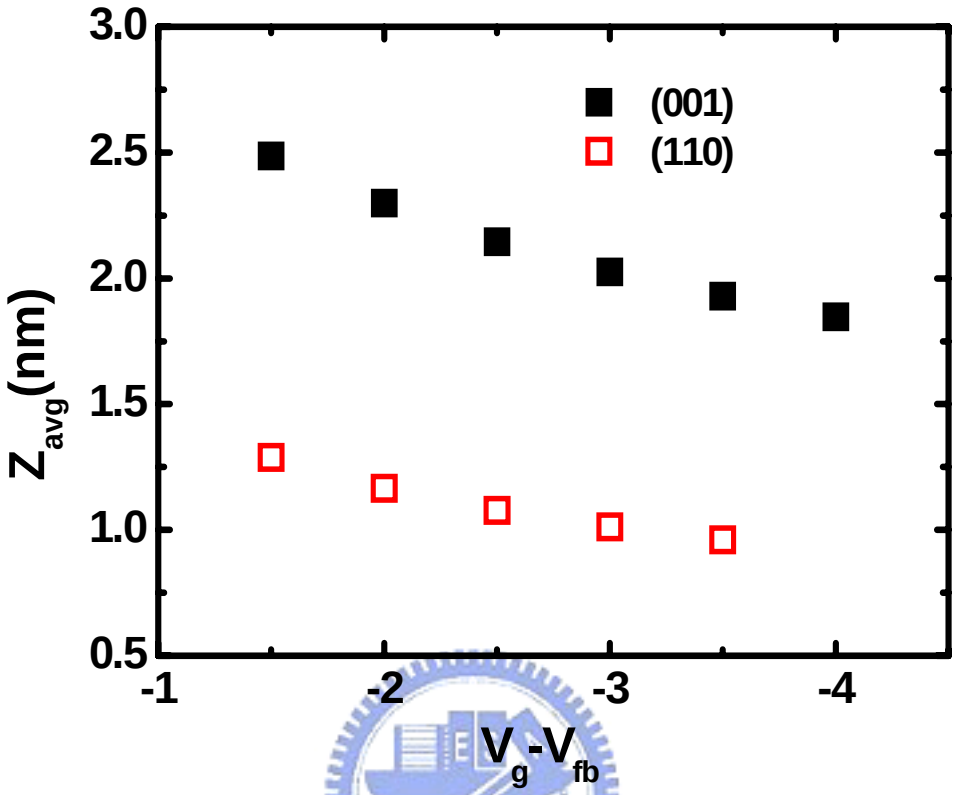

Fig. 3.17 Z_{avg} of the inversion layer as a function of gate bias on (001) and (110) Si substrates.

Chapter 4

Self-consistent Simulation of Quantization Effects in Double Gate and Single Gate MOS

4.1 Introduction

The double-gate (DG) transistor, where the both gates are employed to control the channel, exhibits attractive advantages in comparison to the conventional MOS transistor. The double gate transistor has the properties of almost ideal subthreshold swing and high transconductance. The increase of DG transistor's current is due to the formation of a double conducting channel close to the two Si and SiO_2 interfaces. The additional advantage in terms of transconductance and current drive are attributed to the inversion layer of the silicon region away from the two interfaces, which suffer less surface roughness scattering. The double-gate transistor with even thinner semiconductor layer can work in the volume inversion regime [4.1-4.3], which means that the whole volume of the semiconductor region is in the strong inversion.

If the semiconductor layer is ultra thin, the energy quantization effect becomes evident which affects considerably the carrier distribution in the semiconductor and influences the transistor parameters. In this chapter, we firstly investigate the effect of the semiconductor thickness on the hole density distribution, threshold voltage and finally compare the double-gate and single-gate transistor in terms of hole density distribution and the effective electric field, which are related to the low field mobility.

4.2 Device Configuration and Simulation Technique

In our simulations, we use the p-type (100) double-gate (DG) and single gate

(SG) MOS devices. The silicon thickness down to 5nm and the thickness of the back-oxide of the SG MOS device 50nm are considered. For the silicon layer, n-type doping with $N_D=10^{17}$ cm^{-3} is assumed for both cases. The two gate electrodes of the DG device and the front gate of the SG are assumed of p^+-polysilicon, while in the SG device a grounded n^+-polysilicon gate mimics the effect of the silicon substrate, as shown in Fig 4.1.

The simulation is carried out by self-consistently solving the Poisson and Schrödinger equations. The quasi-Fermi levels for electrons and holes are set within the whole simulation domain, to reflect a bias condition with grounded source and drain. The poly depletion and wave function penetration into the gate oxide are neglected in our simulations. The procedures of solving the Poisson and Schrödinger equations are referred to chapter 3.

4.3 Results and Discussions

4.3.1 Symmetric Double Gate MOS

Fig. 4.2 shows the hole concentration distribution in a DG MOS device with 10nm silicon thickness and 6nm oxide, which is biased above threshold. A maximum at the center of the silicon layer is obtained at lower gate voltage, while at higher gate voltage two inversion maxima are formed. The effect of volume inversion vanishes rapidly as silicon thickness is increased, resulting in a reduction of the minority carrier concentration in the middle of the silicon layer.

Fig. 4.3 shows the influence of the silicon thickness on the hole concentration distribution at the same V_g-V_{fb}. As shown in Fig. 4.3, if the silicon thickness is thinner than 10nm, two regions overlap strongly that the hole concentration maximum is located in the middle of the silicon layer, and the distribution is totally different

from the classical picture. In Fig. 4.4, the dependence of the total inversion hole density on the different silicon thickness in the symmetrical DG device is shown. For the small V_g-V_{fb}, i.e. small surface potential, when the potential is nearly rectangular, the quantization is effective only for silicon thickness thinner than 20nm, as a result of the hole wave functions confinement by the two silicon and oxide interfaces. On the other hand, for the larger V_g-V_{fb}, all holes are confined in the surface subwells. As a consequence, the inversion hole density does not depend on the silicon thickness.

Fig. 4.5 shows the dependence of the threshold voltage on the silicon thickness T_{si}. The threshold voltage is determined by the linear extrapolation of the gate voltage dependence of the inversion hole density [4.4]. It is worth noticing that the turn-around characteristic of the threshold voltage is demonstrated, which implies that for silicon layer thickness below 20nm, the effects of surface inversion layer overlap and the hole energy quantization become obvious. On the other hand, an appropriate work function of the double gate should be chosen to adjust the positive threshold voltage of pFET demonstrated here.

4.3.2 Comparison of Double Gate and Single Gate MOS devices

In this section, we will focus on the advantages of DG devices in comparison to SG devices in terms of the low-field mobility, which is determined by the transverse electric field in the silicon layer and the displacement of the peak hole concentration from the oxide interface.

In Fig. 4.6, the inversion hole density as a function of the gate voltage in a DG and SG MOS device with 20nm silicon thickness and 3nm oxide is shown. The inset is the linear scale of the inversion hole density versus the gate voltage to extrapolate the threshold voltage. Both two devices show ideal subthreshold swing, which is about 60mV/decade. The DG device also exhibits larger inversion hole charges than

in SG device due to the formation of the two conducting channels. In Fig 4.7 (a), the hole concentration distribution of a DG device is compared to that of a SG device biased with the same gate drive, which means the difference of the threshold voltage of the two devices is considered. The calculated inversion hole density is $7.32*10^{12}$ cm^{-2} for a DG device and $3.65*10^{12}$ cm^{-2} for a SG device, respectively. The inversion hole density of a DG device is twice of a SG device. As shown in the Fig. 4.7 (b), the DG inversion hole density distribution is more displaced from the interface than the SG one, which is about 0.45nm. This difference is crucial in determination of the low-field mobility. Finally, Fig. 4.8 compares the transverse electric field within one half of the silicon layer of a DG and a SG device biased at the same gate drive. The transverse electric field is lower in the DG device and vanishes at the middle of the silicon layer due to the symmetry of the structure. Moreover, the surface roughness scattering rate is given by [4.5],

$$\Gamma_{SR}(k) = \frac{\pi m^* \Delta^2 L^2 e^2}{2\varepsilon s \hbar^3} e^{-(k^2L^2)/2} I_0\left(\frac{k^2L^2}{2}\right) E_{eff}^2 \propto \Delta^2 \cdot E_{eff}^2$$

where $\triangle$ is the average displacement of the interface and E_{eff} is the effective electric field. In a consequence, the effective electric field is lower in the DG device, which possibly results in the improved mobility as a result of a reduction of the surface roughness scattering.

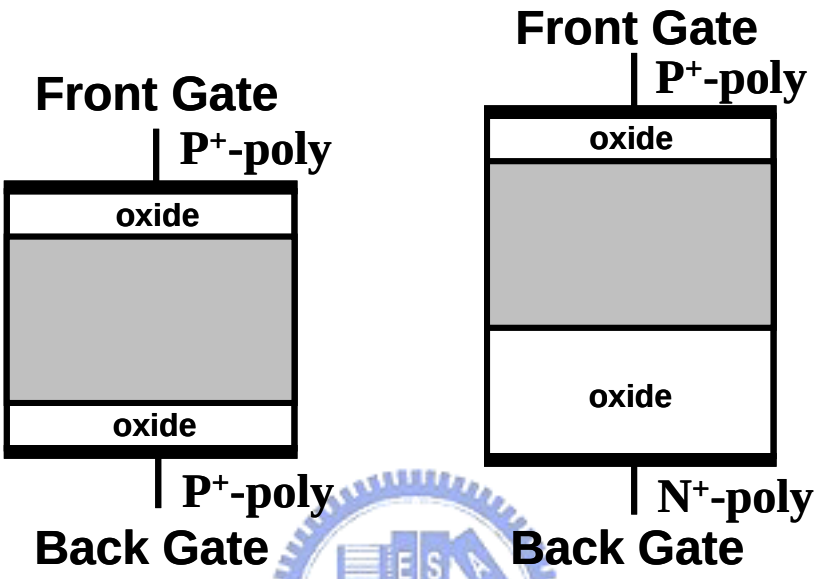

Fig. 4.1 Schematic section of the simulated structures; left: double gate MOS, right: single gate MOS.

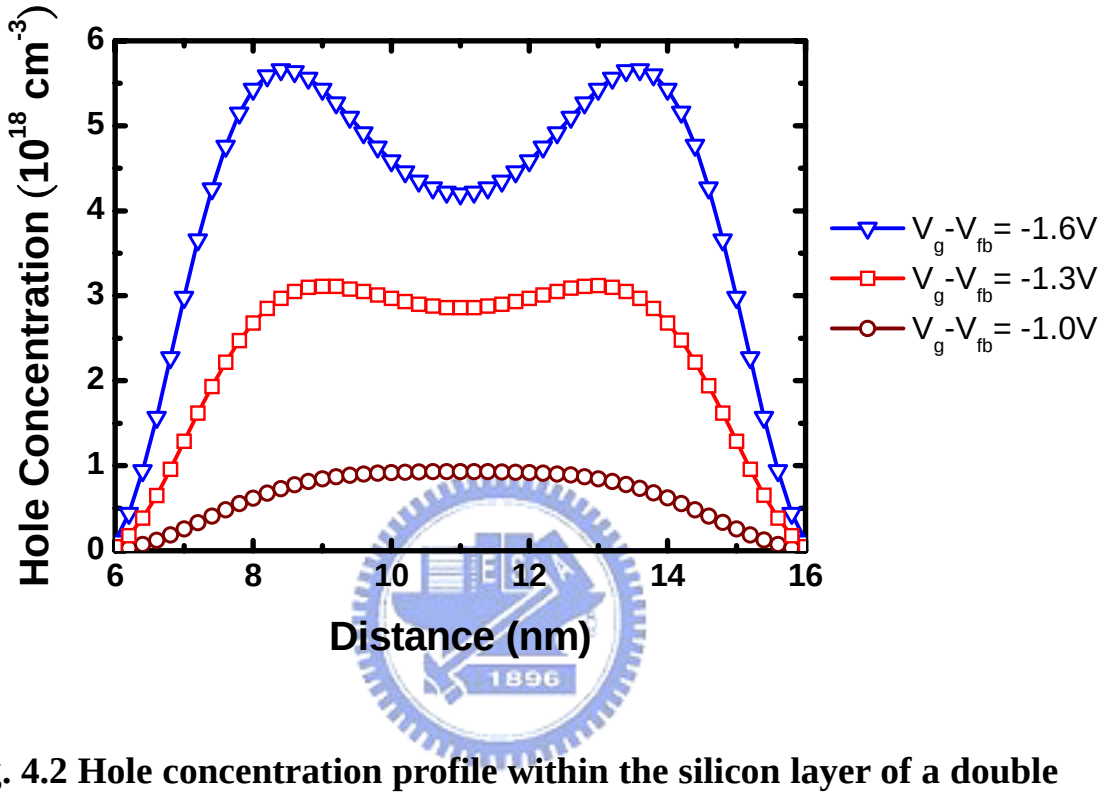

Fig. 4.2 Hole concentration profile within the silicon layer of a double gate MOS with Tsi=10nm, Tox=6nm, for three different bias points above threshold.

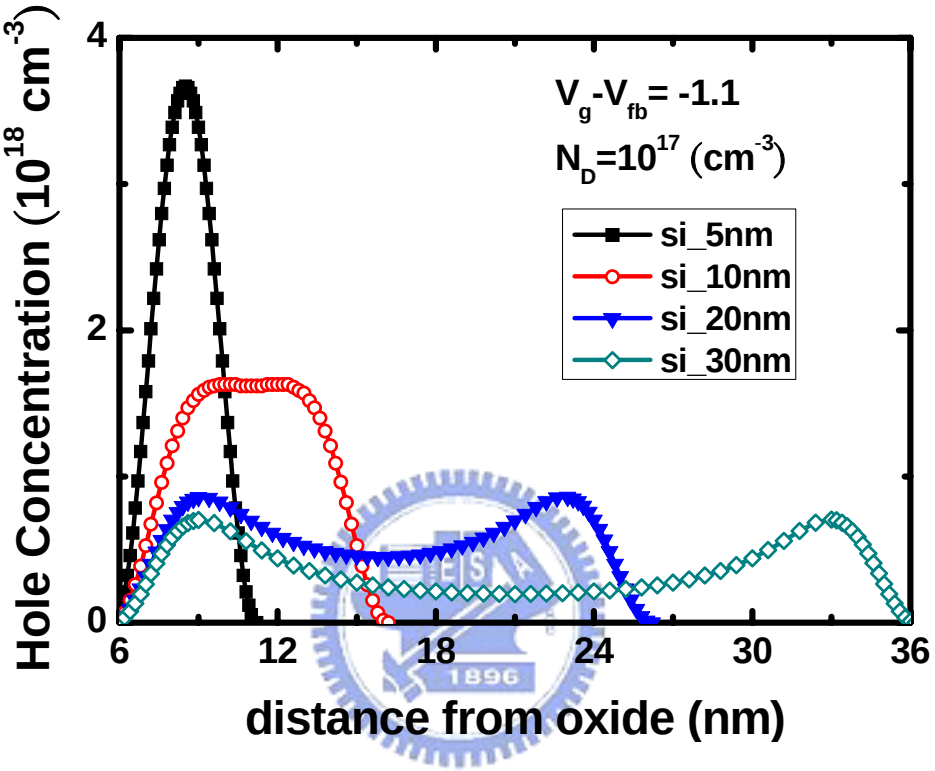

Fig. 4.3 Influence of the silicon thickness on the hole concentration distribution at the same V_g-V_{fb}.

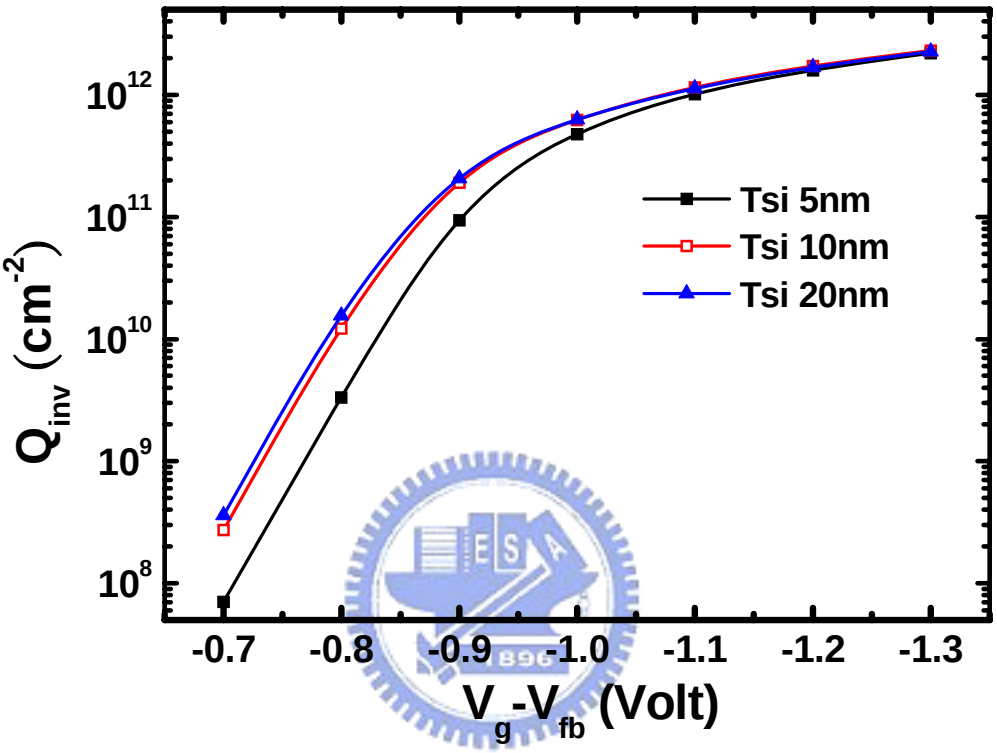

Fig. 4.4 The dependence of the total inversion hole density in the symmetrical DG device on the different silicon thickness.

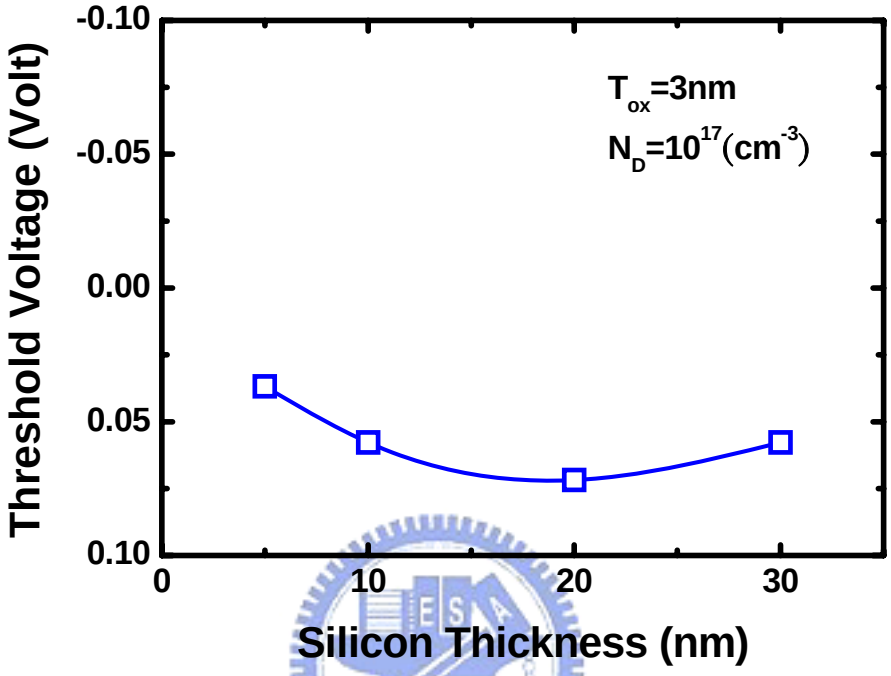

Fig. 4.5 The dependence of the threshold voltage on the silicon layer thickness,Tsi.

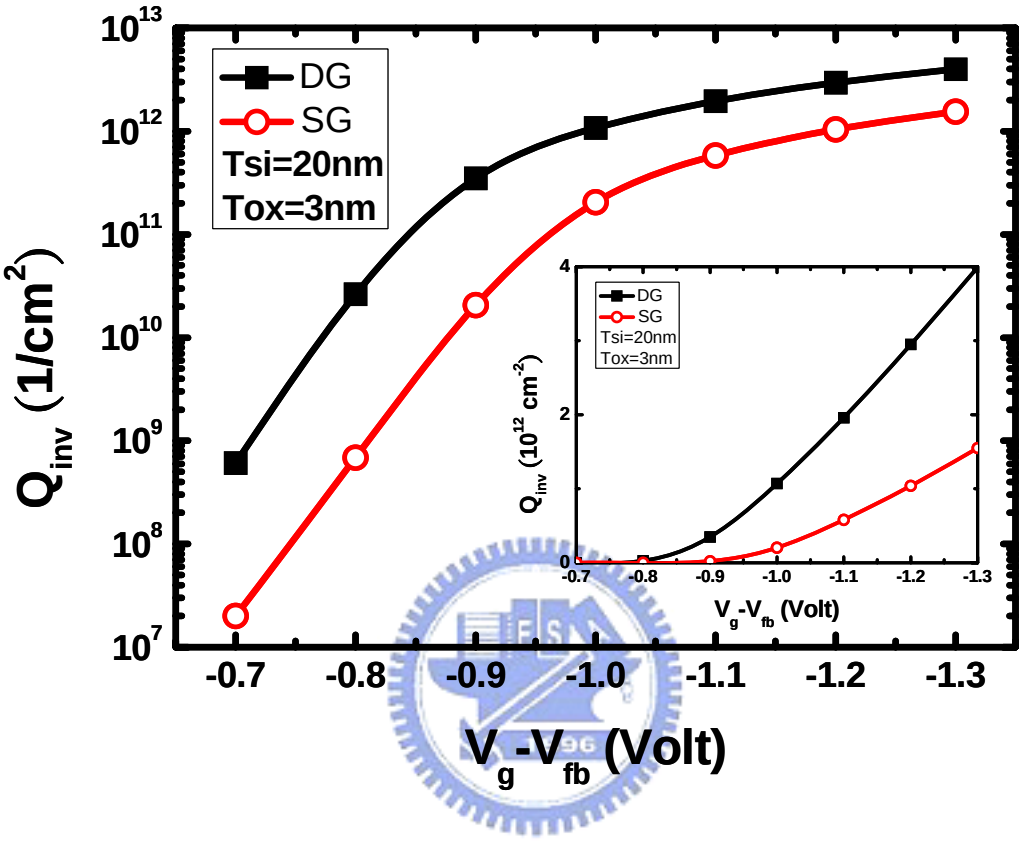

Fig. 4.6 The inversion hole density as a function of gate bias in a DG and SG device with Tsi=20nm and Tox=3nm.

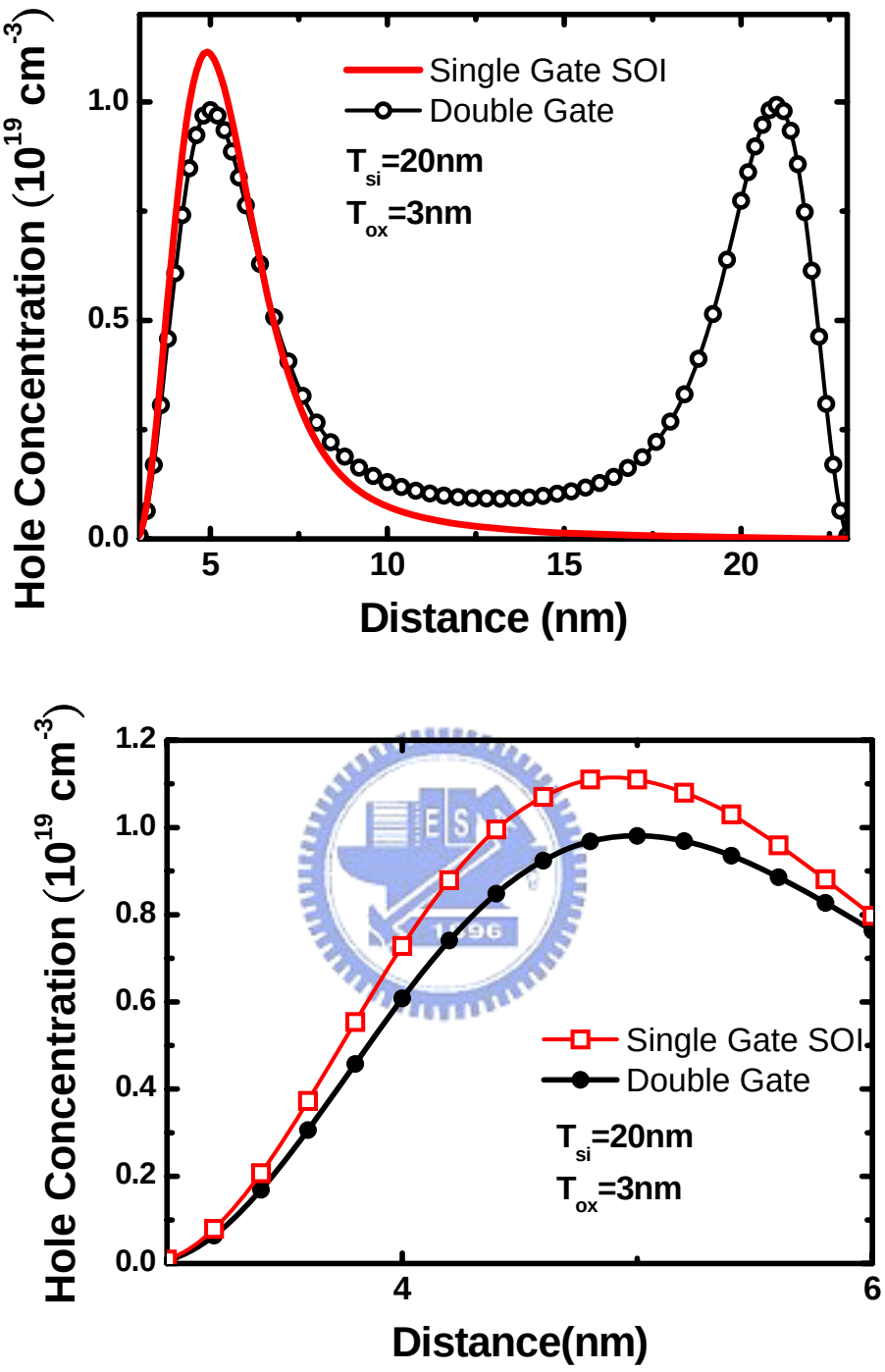

Fig. 4.7 The hole density distribution of a DG device is compared to that of a SG device with Tsi=20nm and Tox=3nm biased with the same gate drive.

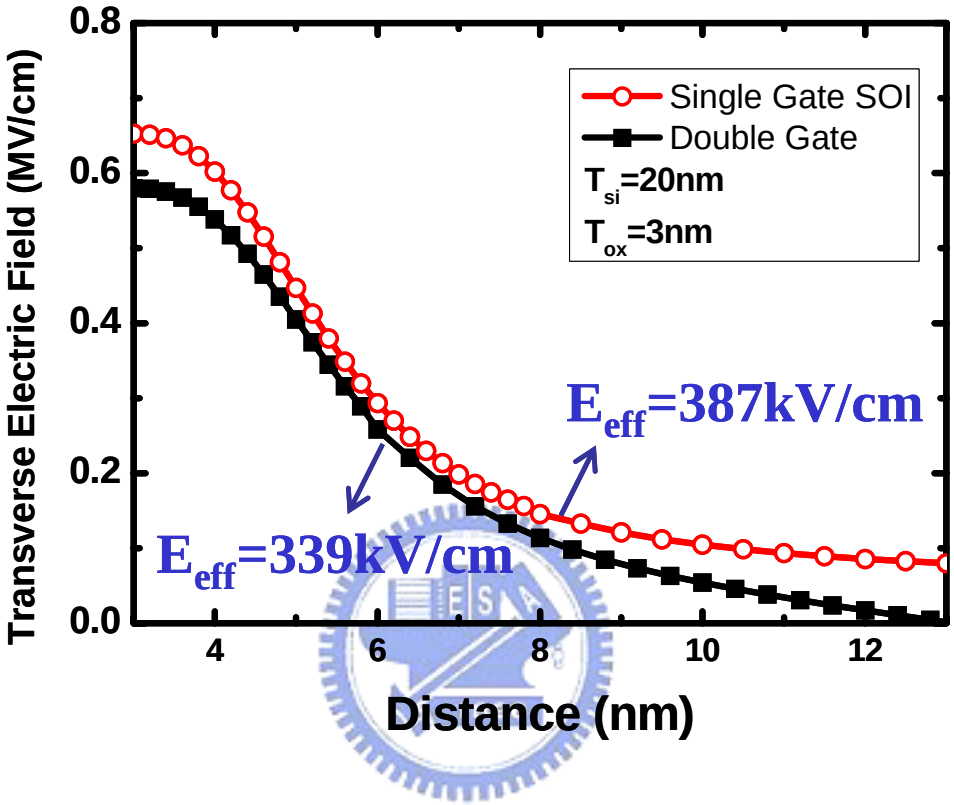

Fig. 4.8 Transverse electric field within one half of the silicon layer of a DG device and a SG one.

Chapter 5

Hole Transport in Si/Ge Quantum Well

5.1 Introduction

Currently, uniaxial compressively strained Si is the dominant technology for high performance pMOSFETs. For further CMOS scaling, it is imperative to investigate other high mobility channel materials, such as Ge and strained Si/Ge, which may possess better carrier transport property than a highly strained Si.

Due to drastic changes in carrier transport theory as CMOS is scaling down beyond 45nm, the traditional device simulator is inadequate to correctly predict the device's performance, such as FinFet, double gate, SOI and so on. As a result, the first principle of the transport theory, Boltzmann transport equation, is needed. The purpose of this chapter is to study the hole transport properties based on the Monte Carlo method. Since the hole scattering rate is closely associated with a hole wave function and a subband structure, the hole mobility may change significantly with the shape of the Si/Ge quantum well geometry. Thus, to obtain a structure-dependent scattering rate, realistic subband structure and hole wave-functions are used in the evaluation of the scattering rate. Tabular forms of the subband E-k structure and scattering rates are established in our Monte Carlo simulation.

5.2 Physical Model and Simulation Technique

Two important scattering mechanisms are considered in the simulation: acoustic phonon scattering and optical phonon scattering. The scattering-matrix elements are approximated, such that phonon scattering can be considered as velocity randomizing.

The square of the matrix elements between the m-th subband and the n-th subband [5.1]:

$$\left|M_{mn}(k_{\|},k_{\|}')\right|_{2D}^{2}=\frac{1}{2\pi}\int\left|M_{3D}(q_x,q_y,q_z)\right|_{3D}^{2}\times\left|\mathrm{I}_{mn,2D}(k_{\|},k_{\|}',q_z)\right|^{2}dq_z$$

Where M_{3D} is the corresponding matrix element for a bulk hole and q is a phonon wave vector. The overlap integral I_{mn} is defined as

$$\mathrm{I}_{mn,2D}(k_{\|},k_{\|}',q_z)=\sum_{\alpha}\int F_{n\alpha}^{*}(k_{\|},z)F_{m\alpha}(k_{\|},z)\exp(iq_z z)dz$$

The coupling coefficient for the two dimensional hole is derived:

$$\begin{aligned}H_{mn}(k_{\|},k_{\|}')&=\frac{1}{2\pi}\int\left|\mathrm{I}_{mn,2D}(k_{\|},k_{\|}',q_z)\right|^{2}dq_z\\&=\int\sum_{\alpha}\sum_{\beta}F_{n\alpha}^{*}(k_{\|}',z)F_{n\beta}(k_{\|}',z)F_{m\alpha}(k_{\|},z)F_{m\beta}^{*}(k_{\|},z)dz\end{aligned}$$

Using the matrix elements, the two dimensional hole scattering rates are calculated according to [5.2]. The acoustic phonon scattering rate is give by

$$S_{ac}=\frac{2\pi k_B T\Xi^{2}}{\hbar\rho u_l^{2}}\cdot D_n(E)\cdot H_{mn}(k_{\|},k_{\|}')$$

where Ξ is the effective acoustic deformation potential, ρ is the material density, u_l is the sound velocity, T is lattice temperature and $D_n(E)$ is the two dimensional density of hole states in n-th subband.

The optical phonon scattering is

$$S_{op} = \frac{\pi (D_t K)_{op}^2}{\rho \omega_{op}^2} \cdot [n_{op} + \frac{1}{2} \mp \frac{1}{2}] \cdot D_n(E \pm \hbar \omega_{op}) \cdot H_{mn}(k_{\|}, k_{\|}^{'})$$

where D_tK is the average optical deformation potential n_{op} is the Bose-Einstein distribution. The + and – represents the absorption and emission rates. The scattering parameters are listed in Table 5.1 [5.3, 5.4].

In the numerical implementation of the valence subband structure in a Monte Carlo simulation, a tabular form of the E-k relationship for the lowest four valence subbbands is established in the simulation. According to the 8-fold symmetry of the Brillouin zone of the subband structure in a quantum well, it's only necessary to tabulate one-eighth of the zone, which is defined as

$$0 \le k_x \le k_y \le 0.3$$

As in [5.5], the eigenvalues for $k_{//} < 0.6\pi/a$, which significantly contribute to the low-field channel mobility, are evaluated. The above k-space region is discretized by mesh points and energy and its gradient at each k point are evaluated. A part of the tabular subband structure form of the k-E relationship is shown in Table 5.2. Table 5.3 lists the E-k relationship including a subband index.

A flowchart of a simple Monte Carlo simulation can be referred to [5.6]. In the Monte Carlo simulation, a sample hole is simulated under an external electric field. It travels freely between two successive scatterings. The free-flight time is determined by using a fixed time technique. During the free flight, the hole is accelerated by the field and its momentum and energy are updated according to the tabular form of the E-k relationship. If a scattering happens, a random number is generated to decide the

responsible scattering mechanism and subband index. Then, the new hole state is chosen according to the tabular form of the E-k relationship. This procedure is continued until the fluctuation due to the statistical uncertainty is less than 1%.

5.3 Results and Discussions

Fig. 5.1 shows the configuration of the simulated devices. The Si/Ge/Si and $Si/Si_{0.75}Ge_{0.25}/Si$ system are compared. The well width of 40Å is used in this simulation. Fig. 5.2 shows the calculated two dimensional density of hole states obtained from the realistic subband structure. Compared to $Si/Si_{0.75}Ge_{0.25}/Si$ system, the Si/Ge/Si system has lower density of states, which suggest higher mobility. In Fig. 5.3, hole velocity and average energy versus electric field in $Si/Si_{0.75}Ge_{0.25}/Si$ system are evaluated. The hole velocity and average energy increase with increasing electric field. The calculated phonon-limited low-field mobility is 422 cm^2/Vs under the assumption of no alloy scattering, as shown in Fig. 5.4.

In Fig. 5.5, the Ge quantum well exhibits higher hole mobility than that in $Si/Si_{0.75}Ge_{0.25}/Si$ system and the calculated phonon-limited low-field mobility is about 890 cm^2/Vs. The temperature dependence of the phonon-limited mobility, μ_{ph}, is also evaluated. The approximated power-law dependence is illustrated by the dashed lines, as shown in Fig. 5.6.

Table 5.1 Scattering parameters for Si and Ge

Parameter	*Si*	*Ge*	*unit*
Ξ	9.2 [5.3]	10.8 [5.4]	*eV*
$D_t K$	13 [5.3]	8.8 [5.4]	$10^8\ {}^{eV}\!/_{cm}$
$\hbar\omega_{op}$	62 [5.3]	38 [5.4]	*meV*

Table 5.2 A tabular form of k-E relationship

k_x	k_y	E	dE/k_x	dE/k_y
0	0	0.0000E+00	0.0000E+00	0.0000E+00
0	0.004	4.2834E-04	0.0000E+00	2.0840E-01
0	0.008	1.7100E-03	0.0000E+00	4.3674E-01
0	0.012	3.8300E-03	0.0000E+00	6.0502E-01
0	0.016	6.7600E-03	0.0000E+00	8.3252E-01
0	0.02	1.0470E-02	0.0000E+00	1.0066E+00
0	0.024	1.4910E-02	0.0000E+00	1.1798E+00
0	0.028	2.0040E-02	0.0000E+00	1.3698E+00
0	0.032	2.5780E-02	0.0000E+00	1.5102E+00
0	0.036	3.2060E-02	0.0000E+00	1.6302E+00
0	0.04	3.8780E-02	0.0000E+00	1.7554E+00
0	0.044	4.5850E-02	0.0000E+00	1.7955E+00
0	0.048	5.3150E-02	0.0000E+00	1.8636E+00
0	0.052	6.0560E-02	0.0000E+00	1.8383E+00
0	0.056	6.7960E-02	0.0000E+00	1.8260E+00
0	0.06	7.5280E-02	0.0000E+00	1.7999E+00
0	0.064	8.2500E-02	0.0000E+00	1.8103E+00
0	0.068	8.9660E-02	0.0000E+00	1.7757E+00
0	0.072	9.6860E-02	0.0000E+00	1.8325E+00
0	0.076	1.0421E-01	0.0000E+00	1.8597E+00
0	0.08	1.1180E-01	0.0000E+00	1.9321E+00
0	0.084	1.1970E-01	0.0000E+00	2.0200E+00
0	0.088	1.2797E-01	0.0000E+00	2.1279E+00
0	0.092	1.3664E-01	0.0000E+00	2.2050E+00
0	0.096	1.4572E-01	0.0000E+00	2.3145E+00
0	0.1	1.5523E-01	0.0000E+00	2.4352E+00

Table 5.3 A tabular form of k-E relationship

k_x	k_y	E	*subband*
0.0000	0.0000	0.0000E+00	1
0.0000	0.0013	4.7530E-05	1
0.0013	0.0013	9.5020E-05	1
0.0000	0.0027	1.9052E-04	1
0.0013	0.0027	2.3787E-04	1
0.0027	0.0027	3.8033E-04	1
0.0000	0.0040	4.2834E-04	1
0.0013	0.0040	4.7548E-04	1
0.0027	0.0040	6.1728E-04	1
0.0000	0.0053	7.6071E-04	1
0.0013	0.0053	8.0754E-04	1
0.0040	0.0040	8.5313E-04	1
0.0027	0.0053	9.4842E-04	1
0.0040	0.0053	1.1800E-03	1
0.0000	0.0067	1.1900E-03	1
0.0013	0.0067	1.2300E-03	1
0.0027	0.0067	1.3700E-03	1
0.0053	0.0053	1.5100E-03	1
0.0040	0.0067	1.6100E-03	1
0.0000	0.0080	1.7100E-03	1
0.0013	0.0080	1.7500E-03	1
0.0027	0.0080	1.8900E-03	1
0.0053	0.0067	1.9300E-03	1
0.0040	0.0080	2.1200E-03	1
0.0000	0.0093	2.3200E-03	1
0.0067	0.0067	2.3500E-03	1

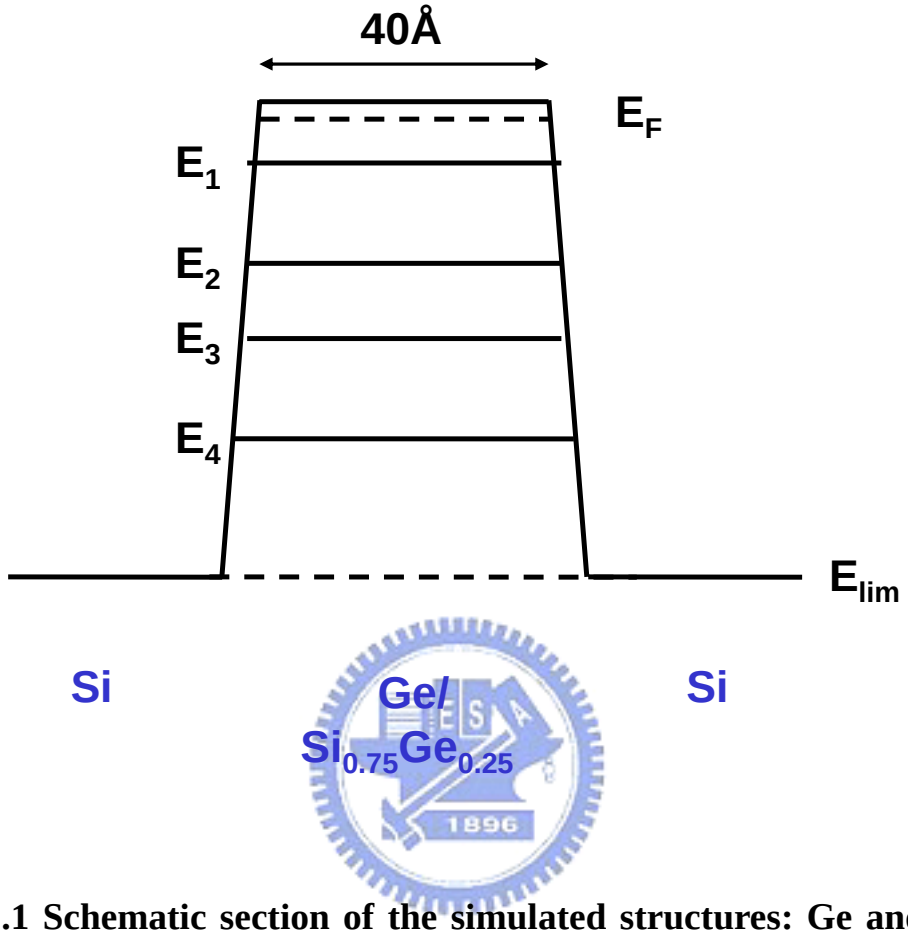

Fig. 5.1 Schematic section of the simulated structures: Ge and SiGe quantum well.

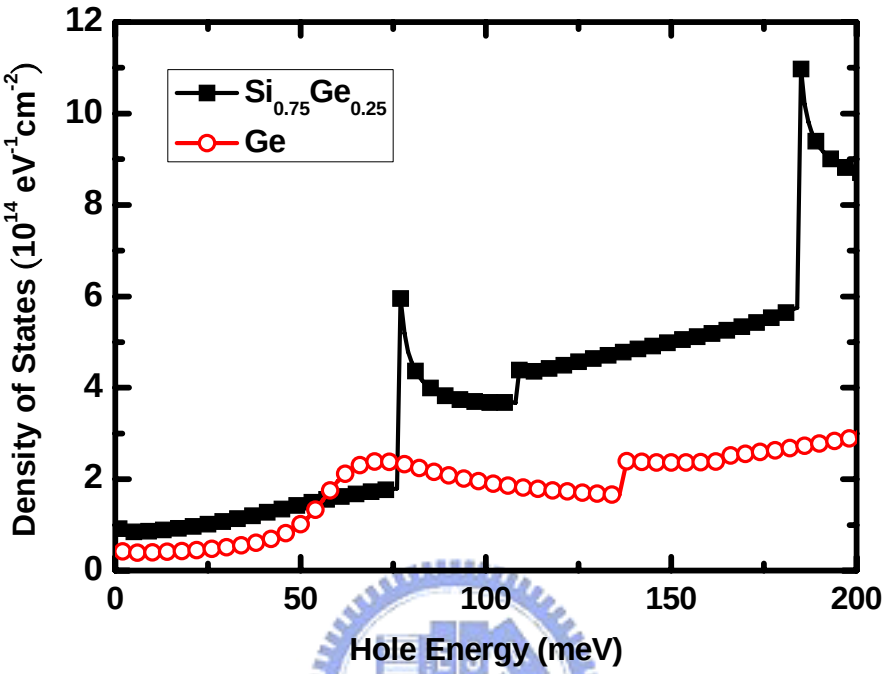

Fig. 5.2 Two dimensional density of states in Ge and SiGe quantum well.

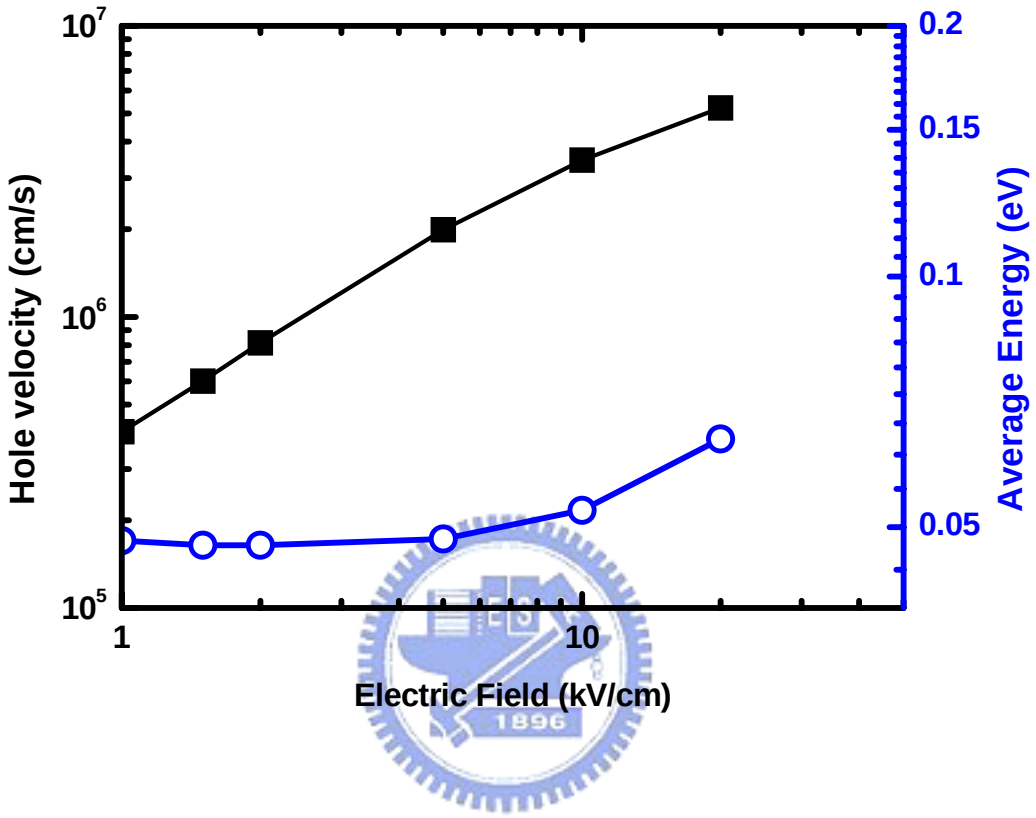

Fig. 5.3 Hole velocity and average energy versus electric field.

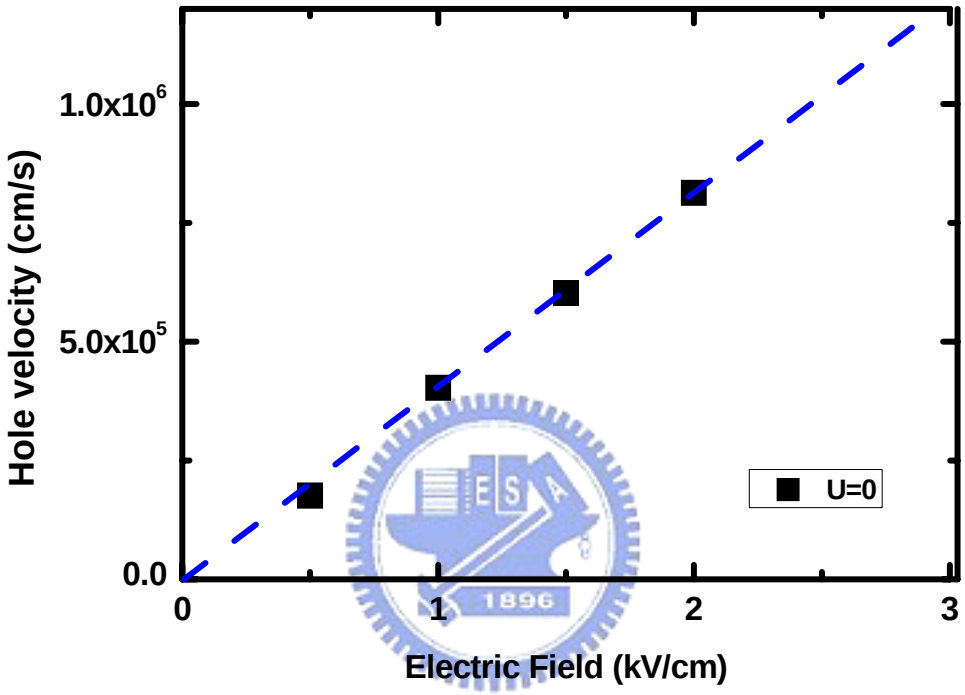

Fig. 5.4 The phonon-limited low-field mobility in SiGe quantum well structure.

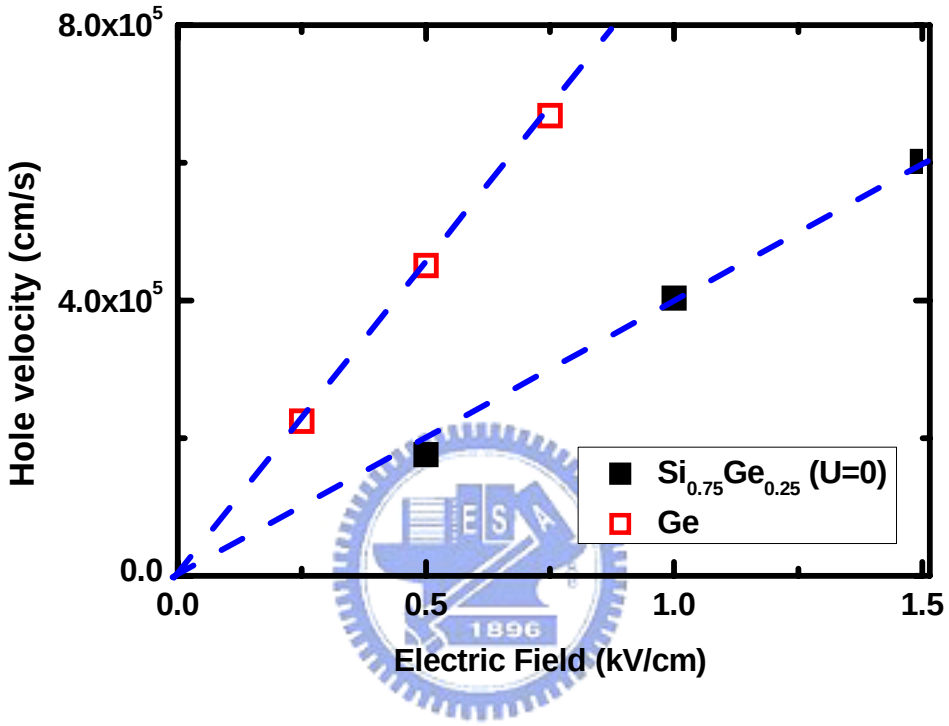

Fig. 5.5 Comparisons of phonon-limited low-field mobility in Ge and SiGe quantum well.

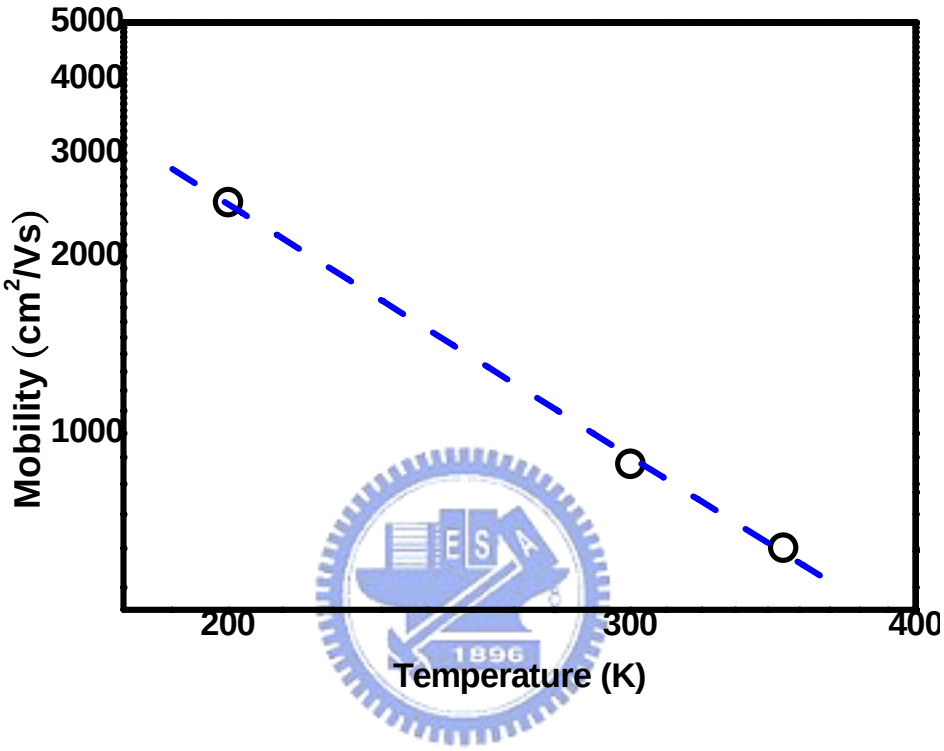

Fig. 5.6 Temperature dependence of the phonon-limited mobility in Ge quantum well.

Chapter 6

Conclusion

In this thesis, a self-consistent solution of the coupled Schrödinger and Poisson equation with the six-band Luttinger-Kohn model is presented. The hole subbands of the inversion layers in p-type MOS, SG SOI and DG devices are demonstrated.

In chapter 2, the Luttinger-Kohn model is introduced. In chapter 3, we have shown the physical characteristics in a (001) and (110) p-type MOS device. The subband energies, wave functions, two dimensional density of states are demonstrated. The applied bias and substrate orientation effects are also included in the simulation. In terms of the inversion layer capacitance, the (110) pMOS device shows higher performance than (001) pMOS device due to smaller peak depth of the hole concentration in the (110) MOS device. In chapter 4, we also have shown that symmetrical DG devices exhibit attractive advantages in comparison to SG SOI devices as a result of the double conducting channels and the improved low-field mobility resulting from the lower effective electric field in the silicon layer. In chapter 5, a two dimensional hole Monte Carlo simulation is developed to study the hole transport in Ge and SiGe quantum wells. The simulation results show that the phonon-limited low-field mobility in Ge quantum well is larger that that in SiGe quantum well due to lower scattering rate and lower effective mass.

References

Chapter 1

[1.1] P. Bai et al., “A 65 nm logic technology featuring 35 nm gate lengths, enhanced channel strain, 8 Cu interconnects layers, low-k ILD and 0.57 um2 SRAM cell,” ***IEDM Technical Digest***, pp. 657–660, 2004.

[1.2] P.R. Chidambaram, B.A. Smith, L.H Hall, H. Bu, S. Chakravarthi, Y. Kim, A.V. Samoilov, A.T. Kim, P.J. Jones, R.B. Irwin, M.J Kim, A.L.P Rotondaro, C.F Machala, and D.T. Grider, “35% drive current improvement from recessed-SiGe drain extensions on 37 nm gate length PMOS,” in Proc. Symp. VLSI Technology, pp. 48–49, 2004.

[1.3] T. Ghani, M. Armstrong, C. Auth, M. Bost, P. Charvat, G. Glass, T. Hoffiann, K. Johnson, C. Kenyon, J. Klaus, B.Mclntyre, K. Mistry, A. Murthy, 1. Sandford, M. Silberstein, S. Sivakumar, P. Smith, K. Zawadzki, S. Thompson and M. Bohr. “A 90 nm high volume manufacturing logic technology featuring novel 45 nm gate length strained silicon CMOS transistors,” ***IEDM Technical Digest***, pp.11.6.1–11.6.3, 2003.

[1.4] V. Chan, R. Rengarajan, N. Rovedo, W. Jin, T. Hook, P. Nguyen, J. Chen, Ed Nowak, X. D. Chen, D. Lea, A. Chakravani, V. Ku, S. Yang, A. Steegen, C. Baiocco, P. Shafer, H. Ng, S. F. Huang, C. Wann. “High speed 45 nm gate length CMOSFETs integrated into a 90 nm bulk technology incorporating strain engineering,” ***IEDM Technical Digest***, pp. 3.8.1–3.8.4, 2003.

[1.5] Kah-Wee Ang, Jianqiang Lin, Chih-Hang Tung, N. Balasubramanian, Ganesh Samudra, and Yee-Chia Yeo, “Beneath-The-Channel Strain-Transfer-Structure (STS) and Embedded Source/Drain Stressors for Strain and Performance Enhancement of Nanoscale MOSFETs,” ***in VLSI Symp. Tech. Dig.***, pp. 42–43,

2007.

[1.6] S.E. Thompson, M. Armstrong, C. Auth, S. Cea, R. Chau, G. Glass, T. Hoffman, J. Klaus, Ma Zhiyong, B. Mcintyre, A. Murthy, B. Obradovic, L. Shifren, S. Sivakumar, S. Tyagi, T. Ghani, K. Mistry, M. Bohr, and Y. El-Mansy," A logic nanotechnology featuring strained silicon," ***IEEE Electron Device Lett.***, vol. 25, pp. 191–193, 2004.

[1.7] M. Passlack, P. Zurcher, K. Rajagopalan, R. Droopad, J. Abrokwah, M. Tutt, Y.-B. Park, E. Johnson, O. Hartin, A. Zlotnicka, and P. Fejes ,"High Mobility III-V MOSFETs For RF and Digital Applications, ***IEDM Technical Digest***, pp. 621-624, 2007.

[1.8] Krishna C. Saraswat, Chi On Chui, Donghyun Kim, Tejas Krishnamohan and Abhijit Pethe," High Mobility Materials and Novel Device Structures for High Performance Nanoscale MOSFETs," ***IEDM Technical Digest***, pp. 1-4, 2006.

Chapter 2

[2.1] M. L. Cohen and T. K. Bergstresser, "Band structures and pseudopotential form factors for fourteen semiconductors of the diamond and zinc-blende structures," ***Phys. Rev.***, vol.141, pp.789,1966.

[2.2] J. R. Chelikowsky and M. L. Cohen, "Nonlocal pseudopotential calculations for the electronic structure of eleven diamond and zinc-blende semiconductors" ***Phys. Rev. B***, vol.14, pp.556,1976.

[2.3] G.Ottaviani, L. Reggiani, C.Canali, F. Nava, and A. Alberigi-Quaranta, "Hole drift velocity in silicon," ***Phys. Rev. B***, vol.12, pp.3318-3329, 1975.

[2.4] S. Krishnamurthy and J. A. Moriarty, "Electronic structure and

impurity-limited electron mobility of silicon superlattices," ***Phys. Rev. B***, vol.32, pp.1027, 1985.

[2.5] Y. C. Chang, "Bond-orbital models for superlattices," ***Phys. Rev. B***, vol.37, pp. 8215-8222, 1988.

[2.6] W. A. Harrison, "Bond orbital model and the properties of Tetrahedrally coordinated solids," ***Phys. Rev. B***, vol.8, pp.4498, 1973.

[2.7] G. L. Bir and G. E. Pikus, Symmetry and strain-induced Effects in Semiconductors, Wiley New York, 1974.

[2.8] Tony Low, M. F. Li, Y. C. Yeo, W. J. Fan, S. T. Ng and D. L. Kwong, "Valence band structure of ultrathin silicon and germanium channels in metal-oxide-semiconductor field-effect transistors," ***J. Appl. Phys***., vol. 98, 024504, 2005.

[2.9] M. V. Fischetti and S. E. Laux, "Band structure, deformation potentials, and carrier mobility in strained Si, Ge, and SiGe alloys," ***J. Appl. Phys***., vol. 80, pp.2234, 1996.

[2.10] J. M. Luttinger and W. Kohn, "Motions of electrons and holes in perturbed periodic field," ***Phys. Rev.***, vol. 97, pp.869, 1955.

[2.11] J. M. Luttinger and W. Kohn, "Quantum theory of cyclotron resonance in semiconductors: general theory," ***Phys. Rev.***, vol. 102, pp.1030, 1956.

[2.12] Y. X. Liu, D. Z.-Y. Ting, and T. C. McGill, "Efficient, numerically stable multiband *k.p* treatment of quantum transport in semiconductor heterostructures," ***Phys. Rev. B***, vol. 54, pp.5675, 1996.

Chapter 3

[3.1] C. Moglestue, “Self-consistent calculation of electron and hole inversion charges at silicon–silicon dioxide interfaces,” ***J. Appl. Phys.***, vol. 59, no. 5, p. 3175, 1986.

[3.2] C.-Y. Hu, S. Banerjee, K. Sadra, B. C. Streetman, and R. Sivan, “Quantization effects in inversion layer of pMOSFETs on Si (100) substrate,” ***IEEE Electron Device Lett.***, vol. 17, pp. 276–278, June 1996.

[3.3] I. H. Tan, G. L. Snider, L. D. Chang, and E. L. Hu, “A self-consistent solution of Schrödinger-Poisson equations using a nonuniform mesh,” ***J. Appl. Phys.***, vol. 68, pp.4071, 1994.

[3.4] J. A. Lo´pez-Villanueva, I. Melchor, F. Ga´miz, J. Banqueri, and J. A. Jime´nez-Tejada, “A model for the quantized accumulation layer in metal-insulator-semiconductor structures,” ***Solid-State Electron.***, vol. 38, pp.203, 1995

[3.5] Yifei Zhang and Jasprit Singh, “Channel effective mass and interfacial effects in Si and SiGe metal-oxide-semiconductor field effect transistor: A charge control model study,” ***J. Appl. Phys..***, vol. 83, pp.4264, 1998

[3.6] Howard C.-H. Wang, Shih-Hian Huang, Ching-Wei Tsai, Hsien-Hsin Lin, Tze-Liang Lee, Shih-Chang Chen, Carlos H. Diaz, Mong-Song Liang and Jack Y.-C. Sun, “High-Performance PMOS Devices on (110)/<111’> Substrate/Channel with Multiple Stressors,” ***IEDM Technical Digest***, 2006

[3.7] J. A. Lo´pez-Villanueva, P. Cartujo-Casinello, J. Banqueri, F. Ga´miz, and S. Rodrı´guez, “Effects of the inversion layer centroid on MOSFET behavior,” ***IEEE Trans. Electron Devices***, vol. 44, pp.1915, 1997.

[3.8] S. Okamoto, K. Miyashita, N. Yasutake, T. Okada, H. Itokawa, I. Mizushima, A. Azuma, H. Yoshimura and T. Nakayama, “Study on High Performance (110)

PFETs with Embedded SiGe," ***IEDM Technical Digest,*** p. 277, 2007.

Chapter 4

[4.1] F. Balestra, S. Cristoloveanu, M. Benachir, J. Brini, and T. Elewa, "Double-gate silicon-on-insulator transistor with volume inversion: a new device with greatly enhanced performance", ***IEEE Electron Device Lett.,*** vol. 8, p. 410, 1987.

[4.2] J.P. Colinge, M.H. Gao, A. Roman-Roddguez, H. Maes, and C. Claeys, "Silicon-on-insulator "gate-all-around device"," ***IEDM Technical Digest,*** p. 595, 1990.

[4.3] D.J. Fkank, S.E. Laux, and M.V. Fischetti, "Monte Carlo simulation of a 30 nm Dual-Gate MOSFET: how short can SI go?" ***IEDM Technical Digest***, p. 553, 1992.

[4.4] Y. Omura, S. Horiguchi, M. Tabe, and K. Kishi, "Quantum-mechanical effects on the threshold voltage of ultrathin SOI nMOSFET's," ***IEEE Electron Device Lett.***, vol. 14, pp. 569–571, 1993.

[4.5] D. K. Ferry, ***Semiconductor Transport***, New York: Taylor & Francis, 2000.

Chapter 5

[5.1] P. J. Price, "Two-dimensional electron transport in semiconductor layers. I. Phonon scattering", ***Ann. Phys.,*** vol. 133, p. 217, 1981.

[5.2] M. V. Fischetti, Z. Ren, P. M. Solomon, M. Yang, and K. Rim, "Six-band k"p calculation of the hole mobility in silicon inversion layers: Dependence on surface orientation, strain, and silicon thickness," ***J. Appl. Phys.,*** vol. 94, p. 1079, 2003.

[5.3] Pham, A.-T., Jungemann, C., and Meinerzhagen, B., “Physics-Based Modeling of Hole Inversion-Layer Mobility in Strained-SiGe-on-Insulator,” ***IEEE Electron Device***, vol. 54, pp. 2174, 2007.

[5.4] T. S. Liou, PhD dissertation.

[5.5] E. X. Wang, P. Matagne, L. Shifren, B. Obradovic, R. Kotlyar, S. Cea, M. Stettler, and M. D. Giles, “Physics of hole transport in strained silicon MOSFET inversion layers,” ***IEEE Trans. Electron Devices***, vol. 53, no. 8, pp. 1840–1851, 2006.

[5.6] C. Jacoboni and L. Reggiani, “The Monte Carlo method for the solution of charge transport in semiconductors with applications to covalent materials,” ***Rev. Mod. Phys.,*** vol. 55, pp. 645, 1983.

簡　　歷

姓名:邱子華

性別:女

生日:民國 73 年 5 月 24 日

籍貫:台灣省屏東縣

地址:台灣省屏東縣屏東市自由路 251 號

學歷:國立交通大學材料科學與工程學系　　91.9-95.6

國立交通大學電子工程研究所碩士班　　95.9-97.6

碩士論文題目:

矽及鍺通道 P 型金氧半電晶體二維量子井模擬

Subband Structures of Silicon and Germanium Channels in P-type Metal-oxide-semiconductor Devices